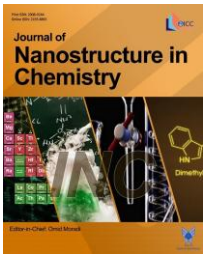

Volume 15, Issue 6, 152522 (1-22)

Journal of Nanostructure in Chemistry (JNSC)

https://doi.org/10.57647/jnsc.2025.1506.22

Chitosan Nanoparticle-Mediated Dual Delivery of Quercetin and Paclitaxel Attenuates EMT and Angiogenesis Via ZEB1 and TIMP-3 Regulation in Triple-Negative Breast Cancer

Hamed Dadashi [1], Amirreza Nazemiyeh [1], Niloufar Ahdeno [1], Parniya Kehtari [1], Samar Mahari[1], Yadollah Omidi[2], Somayeh Vandghanooni[3,*], Morteza Eskandani[1,*]

[1] *Research Center for Pharmaceutical Nanotechnology, Biomedicine Institute, Tabriz University of Medical Sciences, Tabriz, Iran*

[2] *Department of Pharmaceutical Sciences, Barry and Judy Silverman College of Pharmacy, Nova Southeastern University, Fort Lauderdale, FL 33328, United States*

[3] *Hematology and Oncology Research Center, Tabriz University of Medical Sciences, Tabriz, Iran*

[*] **Corresponding authors:** vandghanoonis@tbzmed.ac.ir, eskandanim@tbzmed.ac.ir

Original Research

Received:
1 August 2025

Revised:
15 September 2025

Accepted:
28 September 2025

Published in Issue:
31 December 2025

Abstract

This study investigates the therapeutic potential of chitosan nanoparticles (Cs NPs) loaded with quercetin (Que) and paclitaxel (PTX) against triple-negative breast cancer (TNBC), focusing on their impact on epithelial-mesenchymal transition (EMT), a critical driver of metastasis, using MDA-MB-231 cells *in vitro* and *in vivo* models. Characterized by an average size of 82–91 nm, a positive zeta potential (+21–27 mV), and high encapsulation efficiencies, the Cs NPs demonstrated potent anti-tumor efficacy. Que-/PTX-loaded NPs significantly enhanced *in vitro* cytotoxicity by inducing late apoptosis. Furthermore, they suppressed cell migration and inhibited mammosphere formation in 3D cultures, effectively countering the invasiveness associated with EMT. Notably, the NPs downregulated ZEB1, a key EMT-promoting transcription factor, and upregulated TIMP-3, an inhibitor of extracellular matrix degradation, thereby attenuating EMT-driven metastasis. The chorioallantoic membrane (CAM) assay revealed a significant reduction in angiogenesis, further supporting their anti-metastatic potential. *In vivo*, BALB/c nude mice with MDA-MB-231 xenografts treated with Que-/PTX-Cs NPs exhibited 71.79% tumor growth inhibition and reduced metastatic spread, with 64.27% NP accumulation in tumors. These results underscore Que-/PTX-Cs NPs as a promising nanotherapeutic strategy for TNBC, effectively targeting tumor growth, EMT-driven metastasis, and angiogenesis through ZEB1 and TIMP-3 regulation.

Keywords: Chitosan nanoparticles; Epithelial-Mesenchymal Transition (EMT); Paclitaxel; Quercetin; Triple-Negative Breast Cancer

Cite this article: Dadashi, H., Nazemiyeh, A., Ahdeno, N., Kehtari, P., Mahari,S., Omidi, Y., Vandghanooni, S., Eskandani, M. Chitosan nanoparticle-mediated dual delivery of quercetin and paclitaxel attenuates EMT and angiogenesis via ZEB1 and TIMP-3 regulation in triple-negative breast cancer Chitosan nanoparticle-mediated dual delivery of quercetin and paclitaxel attenuates EMT and angiogenesis via ZEB1 and TIMP-3 regulation in triplenegative breast cancer. *J Nanostruct Chem* **15**(06), 152522 (2025).

1.Introduction

Cancer remains a critical global health challenge, primarily due to its poor prognosis. Among various cancer types, breast cancer is particularly prevalent in women[1, 2], and demands urgent intervention post-diagnosis. A patients undergoing conventional therapies such as surgery, chemotherapy, and radiotherapy [4] . Chemotherapy often induces off-target effects, including severe cardiac [5] , hepatic [6] , and renal [7] complications, which significantly impair patients' quality of life. To enhance therapeutic outcomes while minimizing adverse effects, nanotechnology offers advanced drug carriers [8] , including carbon-based [9] , metallic [10, 11], lipid-based [12-14], and natural [15, 16] or synthetic polymer-based [17-19] Nanoparticles (NPs). Despite improved anticancer efficacy, certain nanoplatforms still carry toxicity risks [20, 21]. An ideal drug carrier should be both safe and efficient, prolonging drug circulation time. In this context, natural polymer-based NPs stand out as biocompatible nanoscale drug delivery systems (NDDSs) with minimal or no toxicity [22-24]. Chitosan (Cs), a cost-effective and abundant natural polysaccharide, is derived from chitin, a key component in the exoskeletons of crustaceans like shrimp and crabs [25, 26]. The deacetylation of chitin introduces valuable amine groups, enabling NP synthesis through ionic gelation or surface modifications. These amine groups also confer a positive charge to Cs NPs, enhancing cellular uptake and endosomal escape [27] . While surface modifications allow for targeted delivery, the unique tumor microenvironment facilitates passive targeting via the enhanced permeability and retention (EPR) effect, making NPs a cost-effective strategy for cancer therapy. Additionally, combining nano-encapsulated chemotherapeutic agents with oligonucleotides, antioxidants, or herbal compounds can reduce required drug doses and enhance synergistic anticancer effects [28-30]. Addressing tumor invasiveness is crucial for successful treatment, which is why this study focuses on MDA-MB-231 triple-negative breast cancer cells (TNBCCs), known for their high metastatic potential and resistance. Here, we explore the anticancer and antimetastatic effects of Cs NPs loaded with paclitaxel (PTX) and quercetin (Que). PTX (Taxol), a lipophilic chemotherapeutic agent with ~90% protein binding, is typically administered intravenously. As a taxane diterpene derived from Taxus plants, PTX inhibits cell division by disrupting microtubule function, but is also associated with cardiac [31] and inflammatory toxicity [32] . Que, a plant-derived flavonol found in vegetables, kale, and red onions, exhibits antioxidant, anticancer, and anti-inflammatory properties [33] but suffers from poor bioavailability and a short half-life. Given the solubility and pharmacokinetic challenges of both PTX and Que, Cs NPs serve as an effective and safe NDDS to overcome these limitations.

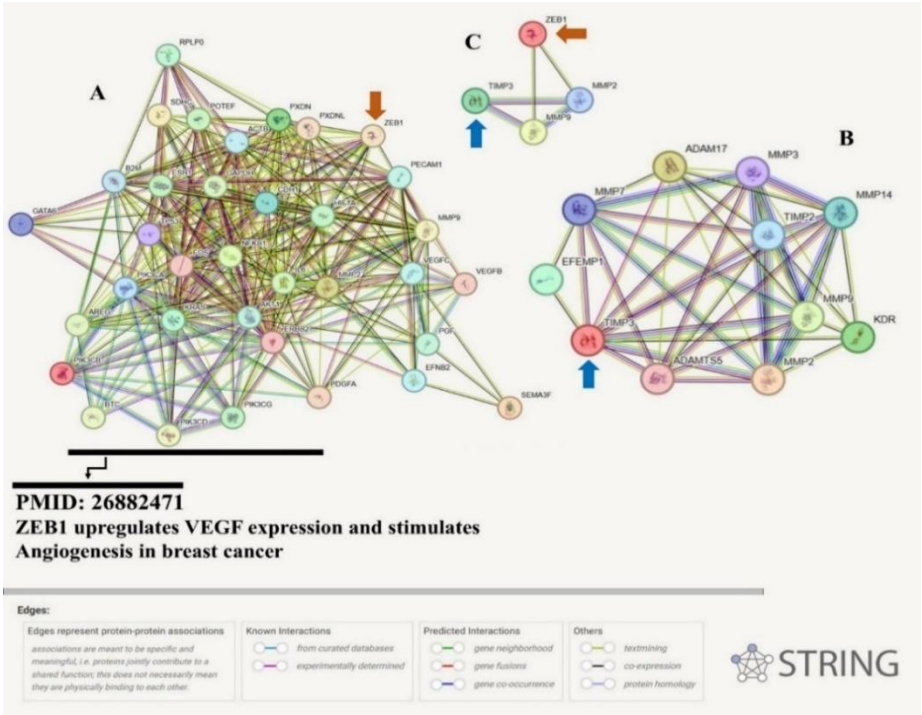

Figure 1. Protein-protein interaction networks involving ZEB1 and TIMP3. (**A**) ZEB1-associated interactions [34] (orange highlights), (**B**) TIMP3 associated interactions (blue highlights), and (**C**) their functional cross-talk Networks were adapted from STRING (v12) under Creative Commons Attribution 4.0 International License (https://string-db.org)

While PTX is a powerful anticancer drug, it may lead to cancer invasiveness [35, 36], whereas Que has demonstrated clear antimetastatic properties [37] . To explore this further, we investigated how the combined Que-/PTX-Cs NP therapy influences the expression of metalloproteinase inhibitor 3 (TIMP3) (a key inhibitor of extracellular matrix degradation via matrix metalloproteinases (MMPs) (figure 1C) , crucial in epithelial-mesenchymal transition (EMT) [38, 39]) and zinc finger E-box-binding homeobox 1 (ZEB1) (a transcription factor linked to E-cadherin suppression and EMT in carcinomas [40 , 41]). As illustrated in Figure 1A, ZEB1 participates in a broad regulatory network, potentially connecting it to angiogenesis-related genes (e.g., Hif-1α, VEGFB, VEGFC), suggesting a possible bridge between EMT and angiogenesis. Additionally, Figure 1B highlights an indirect relationship between TIMP3 and ZEB1, mediated by MMP2 and MMP9.

We hypothesize that Que- and PTX-loaded Cs NPs will demonstrate enhanced anti-tumor, anti-metastatic, and anti-angiogenic effects against MDA-MB-231 triple-negative breast cancer (TNBC) by potently suppressing EMT, a key driver of metastasis. We propose that these NPs, leveraging their optimized nanoscale properties and high drug encapsulation efficiency, will synergistically inhibit tumor cell proliferation, migration, and angiogenesis by modulating critical EMT regulators, specifically by downregulating ZEB1 to disrupt mesenchymal traits and upregulating TIMP-3 to inhibit extracellular matrix degradation. This dual-drug nanoplatform is expected to effectively target tumor growth and EMT-driven metastatic processes in both in vitro and in vivo models, while achieving tumor-specific delivery and minimal systemic toxicity, positioning it as a promising therapeutic strategy for TNBC.

2. Materials and Methods

2.1. Materials

PTX (product code: T7191), Que (product code: Q4951), 3-(4, 5-dimethylthiazol-2-yl)-2,5-diphenyltetrazolium bromide (MTT) (product code: 475989), low molecular weight Cs (approximately 50 kDa, 80% deacetylation degree) (product code: 900341), trypsin-EDTA solution (product code: T4049) and phosphate buffered saline (PBS) (product code: 79382) were acquired from Sigma-Aldrich (St. Louis, MO, USA). Fetal bovine serum (FBS) (product code: 16000044), RPMI-1640 culture medium (product code: 11875093), and penicillin-streptomycin antibiotic mixture (product code: 15140122) were supplied by Gibco Life Technologies (Waltham, MA, USA). Additional chemicals, including acetic acid (product code: 100063), sodium tripolyphosphate (TPP) (product code: 106999), hydrochloric acid (HCl) (product code: 100317), sodium hydroxide (NaOH) (product code: 106498), and other analytical grade solvents and reagents, were procured from Merck Millipore (Burlington, MA, USA).

2.2. Synthesis of chitosan nanoparticles (Cs NPs)

2.2.1 *Preparation of drug-free Cs NPs*

Drug-free Cs NPs were synthesized via ionic gelation following an adapted literature protocol with modifications [25] . Briefly, separate solutions of TPP (0.25% w/v, pH 4.5) and Cs (0.25% w/v, pH 4.5) were prepared, with Cs being dissolved in 1% (v/v) acetic acid aqueous solution. The TPP solution was then gradually added dropwise to the chilled Cs solution under continuous stirring, maintaining a TPP-to-Cs ratio of 1:4.5. Subsequently, the resulting suspension underwent sonication using a Sonopulse homogenizer (Bendelin, Berlin, Germany) - first at 60% amplitude for 2 minutes, followed by 1 minute at 80% amplitude. Since sonication can cause heating, the samples were kept on ice to prevent overheating. The final NPs suspensions were stored at 4°C for further use.

2.2.2 *Preparation of paclitaxel-loaded chitosan nanoparticles (PTX-Cs NPs)*

Initially, a PTX solution (0.15% w/v) was prepared using absolute ethanol as solvent. This PTX solution was then gradually added dropwise during the TPP solution incorporation. Following this addition, the resulting suspension underwent ultrasonic treatment at 60% amplitude for 2 minutes. The NPs were then purified through centrifugation (14,000 ×g, 30 minutes ×2), after which the collected pellet was reconstituted in 10 mL deionized water. Finally, the resuspended NPs received additional ultrasonic processing at 80% amplitude for 2 minutes to ensure proper dispersion.

2.2.3 *Preparation of quercetin-loaded chitosan nanoparticles (Que-Cs NPs)*

Que-Cs NPs were synthesized following an optimized version of the established ionic gelation method [42]. The preparation process began with creating a Que solution (0.12% w/v) in absolute ethanol, which was then introduced dropwise concurrently with the TPP solution. The resulting NP suspension subsequently underwent ultrasonic homogenization at 60% amplitude for 2 minutes. Particle purification was achieved through centrifugation (14,000 ×g, 30 minutes ×2), followed by redispersion of the NP pellet in 10 mL deionized water. A final ultrasonication step at 80% amplitude for 3 minutes was performed to ensure homogeneous NP dispersion.

2.2.4 *Preparation of quercetin-loaded chitosan nanoparticles (Que-Cs NPs)*

Que-Cs NPs were synthesized following an optimized version of the established ionic gelation method [42]. The preparation process began with creating a Que solution (0.12% w/v) in absolute ethanol, which was then introduced dropwise concurrently with the TPP solution. The resulting NP suspension subsequently underwent ultrasonic homogenization at 60% amplitude for 2 minutes. Particle purification was achieved through centrifugation (14,000 ×g, 30 minutes ×2), followed by redispersion of the NP pellet in 10 mL deionized water. A final ultrasonication step at 80% amplitude for 3 minutes was performed to ensure homogeneous NP dispersion.

2.2.5 *Preparation of sulforhodamine B-loaded chitosan nanoparticles (SRB-Cs NPs)*

SRB-loaded Cs NPs were fabricated using a modified version of the blank NP preparation protocol. The key modification involved pre-dissolving SRB powder (0.25 mg/mL) in the Cs solution prior to TPP addition. All subsequent processing steps mirrored those employed for unloaded Cs NPs.

To eliminate unencapsulated SRB, the NP suspension underwent centrifugation (14,000 ×g, 30 min) followed by distilled water washing. The final NP pellet was then reconstituted in 10 mL of distilled water.

2.3. Characterization of the prepared NPs

2.3.1 *Size and surface charge*

The particle size, zeta potential, and polydispersity index (PDI) were measured by using a Nanotrac wave (Montgomeryville, PA, USA). Samples were diluted with distilled water (1:20) at 4°C. The hydrodynamic diameter, surface charge (zeta potential), and size distribution (polydispersity index, PDI) of the NPs were determined using a Nanotrac Wave analyzer (Montgomeryville, PA, USA). For measurements, NP samples were diluted with distilled water (1:20) and analyzed at 4°C.

2.3.2 *Morphology*

The surface morphology of Cs NPs was examined using field-emission scanning electron microscopy (FE-SEM; model MV2300, Brno, Czech Republic). For imaging, 150 µL of diluted NP suspension was deposited onto glass slides and allowed to air-dry. Before imaging, samples were sputter-coated with a thin gold layer using a DC sputter coater (Emitech K450X, UK) employing physical vapor deposition (PVD) technology. NP dimensions were subsequently analyzed from the acquired SEM micrographs using ImageJ software (version 1.45, National Institutes of Health, Bethesda, MD, USA).

2.3.3. *Drug-entrapment efficiency of prepared NPs*

To evaluate drug encapsulation, NP suspensions were centrifuged (14,000 ×g, 30 min, 10°C) twice, and the supernatant containing unloaded drug was analyzed using a Cecil UV-Vis spectrophotometer (Cambridge, UK). Measurements were performed at experimentally determined λmax values: 230 nm (PTX), 374 nm (Que), and 563 nm (SRB). Standard calibration curves were constructed for each compound, and drug concentrations in the supernatant were calculated using their respective linear regression equations. Encapsulation efficiency (EE%), drug loading (DL), and drug content (DC%) were then determined using the following equations:

$$EE\% = 100 \times \frac{Total\ drug - (unloaded\ drug)}{Total\ drug}$$

$$DL\ (\frac{mg}{g}) = \frac{Total\ drug\ (mg)}{Drug\_loaded\ NP\ mass\ (g)}$$

$$DC\% = 100 \times \frac{Total\ drug - (unloaded\ drug)}{Drug\_loaded\ NP\ mass}$$

2.3.4. *Fourier transform infrared (FTIR) spectrophotometry*

The chemical composition of unloaded, PTX-loaded, and Que-loaded Cs NPs was characterized by Fourier transform infrared (FTIR) spectroscopy (Bruker, Germany). Spectra were acquired in the range of 400-4000 cm-1 with a resolution of 4 cm-1. For comparative analysis, the following samples were prepared: pure Cs powder, unformulated PTX, unformulated Que, blank Cs NPs, PTX-Cs NPs, and Que-Cs NPs. Prior to analysis, NP suspensions were subjected to two cycles of centrifugation (14,000 ×g, 10°C, 30 min) to collect the NP pellets.

2.3.5. *Cumulative drug release and drug release kinetics*

The cumulative release of PTX and Que from Cs NPs was evaluated using dialysis bags (12 kDa MWCO) under sink conditions at 37°C in two pH environments (7.4 and 5.7). The release media consisted of PBS (pH 7.4) and phosphate buffer (PB, pH 5.7), both containing 0.1% (v/v) Tween 80 to enhance drug solubility.

Prior to the experiment, dialysis membrane permeability was verified using free drugs. For the release study, 4 mL of drug-loaded Cs NP suspension was loaded into dialysis bags and immersed in 40 mL of pre-warmed sink solution under continuous agitation (100 rpm). At predetermined intervals, 2 mL of the release medium was

sampled and replaced with fresh buffer to maintain sink conditions. The drug concentration in the collected samples was quantified by UV-Vis spectrophotometry. To analyze release kinetics, experimental data were fitted to various mathematical models, including zero-order, first-order, Higuchi, Hixon-Crowell, and Korsmeyer-Peppas equations, to determine the predominant release mechanism for each formulation.

2.3.6. *Stability of the prepared NPs*

The physicochemical stability of the NPs was evaluated following 3 months of storage at 4°C. Key parameters, including drug leakage, crystalline structure, particle size, and zeta potential, were analyzed and compared with freshly prepared NPs. For crystalline phase analysis, samples were air-dried on glass slides (1 cm2 surface area) and examined using an X-ray diffractometer (Tongda TD-3700, Dandong, Liaoning, China).

2.4. Investigation of cellular uptake and antitumoral effects of PTX-/ Que-Cs NPs on MDA-MB-231 cells

2.4.1. *Cell culture*

MDA-MB-231 human breast cancer cells (passage numbers 20-22) were obtained from the Pasteur Institute of Iran (Tehran, Iran). The cells were maintained in RPMI-1640 growth medium supplemented with 10% (v/v) fetal bovine serum, 100 units/mL penicillin, and 100 µg/mL streptomycin. Cultures were incubated in a humidified atmosphere containing 5% CO2 at 37°C.

2.4.2. *Cellular uptake*

For quantitative analysis using flow cytometry, cells were plated in 6-well plates at a density of 4×105 cells/well and allowed to adhere for 24 hours. Following incubation, cells were exposed to either free SRB or SRB-loaded Cs NPs (20 µg/mL) for varying time intervals (1-4 hours). Post-treatment, cells were washed thrice with PBS, trypsinized, and collected by centrifugation (300 ×g, 6 minutes). Cell pellets were resuspended in PBS for analysis using a BD FACSCalibur flow cytometer (San Jose, CA, USA) equipped with appropriate fluorescence filters.

For microscopic evaluation, cells were seeded in 24-well plates and cultured for 24 hours prior to treatment with free SRB or SRB-Cs NPs (20 µg/mL) at identical time points. After treatment, cells underwent three PBS washes followed by fixation with 4% paraformaldehyde for 45 minutes at room temperature (24±2°C). Fluorescence imaging was conducted using a BioTek Cytation 5 Cell Imaging Multimode Reader (Agilent Technologies, Santa Clara, CA, USA).

2.4.3. *Cytotoxicity*

Cellular viability and proliferation were evaluated using the MTT colorimetric assay. MDA-MB-231 cells were plated in 96-well plates at a density of 1×104 cells/well and allowed to adhere for 24 hours. Cells were then exposed to varying concentrations of blank Cs NPs, PTX, Que, and the combination of PTX and Que, with complete media serving as the negative control. Following treatment, the medium was replaced with MTT solution (0.5 mg/mL) and incubated for 4 hours. The formazan crystals were subsequently dissolved in DMSO, and absorbance was measured at 570 nm using a RayBiotech Stat Fax 4200 microplate reader (Norcross, GA, USA). For the cytotoxicity evaluation of blank Cs NPs, which contained no PTX, a solution of 5% (v/v) DMSO in complete media was used as the positive control. The synergistic potential of drug combinations was quantitatively assessed using CompuSyn software (v1.0, ComboSyn, Inc.), which calculated both the fraction affected (Fa) representing treatment efficacy and the combination index (CI) characterizing drug interactions. The CI values were interpreted as follows: synergistic effect ($CI \leq 0.9$), additive effect ($0.9 < CI < 1.1$), or antagonistic effect ($CI \geq 1.1$). Based on the software's computational analysis, the Fa50 value (50% affected fraction) obtained regarding the data of 48 hours post-treatment was selected as the optimal benchmark for subsequent experimental evaluations.

2.4.4 *Apoptosis-necrosis test and nucleus morphology evaluation*

In short, cells were plated in 6-well plates at a density of 4 × 105 cells/well and allowed to adhere for 24 hours before treatment. They were then exposed to various samples (including combinations of free Que and PTX as well as Que-/PTX-loaded Cs NPs) for 48 hours. Untreated cells served as the negative control. Following treatment, the cells were detached, washed, and stained with Annexin V-FITC and PI using the Immunostep kit (Salamanca, Spain) following the manufacturer's protocol. Briefly, after detachment, the cells were washed three times with PBS via centrifugation (300 ×g, 6 minutes, 10°C), resuspended in binding buffer (containing 0.1 M Hepes (pH 7.4), 1.4 M NaCl, and 25 mM $CaCl_2$), and stained with Annexin V-FITC and PI for 20 minutes. Fluorescence intensity was measured for 10,000 events using flow cytometry, and data were analyzed with Flowing Software (v2.0, Turku Bioscience, Finland). Additionally, nuclear morphological changes were assessed via DAPI staining. Cells were seeded in 24-well plates (1 × 105 cells/well), allowed to attach for 24 hours, and then treated with different samples (free drug combinations or Que-/PTX-Cs NPs) for 48 hours. After treatment, the medium was removed, and cells

were fixed with 4% paraformaldehyde for 2 hours at room temperature (24 ± 2°C). Following PBS washes, cells were permeabilized with 0.5% Triton X-100 for 3 minutes, stained with DAPI (20 ng/mL) for 20 minutes, and washed again. Nuclear morphology was examined using a BioTek Cytation 5 imaging system (Agilent Technologies, USA). For quantification, the ImageJ software was used to assess nuclear area based on a method by Jon R. Eidet [43] . Briefly, micrographs were converted to 8-bit images, threshold-adjusted for clear nuclei visualization, and non-nuclear fragments were removed. Nuclei were separated using the "Watershed" function and analyzed via the "Analyze Particles" tool, with 100 nuclei evaluated per treatment (n = 100). Results were expressed as nuclear area normalized to the negative control.

2.4.5. *In vitro cell migration assessment*

Cell migration analysis was performed to assess the invasiveness of cells after treatment with various drugs, along with a negative control. Briefly, cells were seeded in 24-well plates at a density of 1 × 105 cells/well. After 24 hours, the medium was removed, and scratches were made in the cell monolayers using a 1000 µL pipette tip. The wells were then washed three times with PBS, followed by treatment with different test samples (e.g., free Que, free PTX, a combination of Que and PTX, Que-loaded Cs NPs, PTX-loaded Cs NPs, and the combined Que-/PTX-Cs NPs). Scratch closure was monitored and quantified using an Olympus CKX41 inverted light microscope (Tokyo, Japan) and Cell^A software (v3.3, Olympus Soft Imaging Solutions GmbH, Germany), with results compared to the negative control. To further evaluate the antimigratory effects of the treatments, total cell coverage in each well was measured using ImageJ software. Additionally, multiple regression plots were generated to analyze the relationship between cell migration, cell coverage, and time.

2.4.6. *3D mammosphere culture and size determination*

To validate the findings from 2D cultures, 3D mammospheres were generated and treated under various conditions to confirm the results. First, a 1% (w/v) agarose solution was autoclaved for sterilization and used to coat the wells of a 96-well plate (40 µL per well). Once solidified and cooled, the plates were seeded with cells (1×104 cells/well) and centrifuged at 300 ×g for 10 minutes. After three days, mammosphere formation was confirmed, and the spheres were treated with different samples (e.g., free Que, free PTX, their combination, Que-Cs NPs, PTX-Cs NPs, and the combined Que-/PTX-Cs NPs), with untreated cells serving as the negative control. Mammosphere imaging and analysis were performed using an Olympus CKX41 inverted light microscope, and micrographs were processed with ImageJ software to assess changes in mammosphere density and size. Although density alterations alone could demonstrate the anticancer effects of the treatments, multiple regression plots incorporating both density and size changes were included to provide a more comprehensive understanding of treatment impact on 3D tumor models. For detailed morphological evaluation, mammospheres from the negative control, free Que+PTX combination, and Que-/PTX-Cs NPs groups were washed with PBS, fixed in 2.5% glutaraldehyde for 4 hours, and then dehydrated using a graded ethanol series (50% to 100% v/v, 30 minutes per step at 4°C). After air-drying, the samples were examined by scanning electron microscopy (SEM) for ultrastructural analysis.

2.5. Angiogenesis investigation

The CAM assay, recognized for its rich vascular network, serves as an established model for evaluating the anti-angiogenic effects of various compounds. All experimental procedures were conducted in strict accordance with the 3Rs principles: Replacement, Reduction, and Refinement to ensure ethical use of animals and to mitigate potential distress or harm. The CAM assay, performed on fertilized chicken embryos, complied with established ethical guidelines and was approved by the same institutional ethics committee overseeing animal protocols. Special attention was given to aligning the study with international standards for embryonic research, emphasizing minimal biological impact. To further uphold animal welfare, the number of embryos utilized was deliberately kept to the lowest possible while maintaining statistical validity, thereby optimizing both scientific rigor and humane practice.For this study, fertilized ROSS 308 chicken eggs were obtained locally and incubated at 37.5°C with 60% humidity until embryonic day 11. On day 10 of development, a small window was carefully created on each egg above a well-vascularized area of the CAM. Sterile discs impregnated with test samples (including the combination of free Que and PTX, and Que-/PTX-loaded Cs NPs) were then applied to the exposed membrane. The eggs were monitored for 48 hours following treatment, with PBS-loaded discs serving as the negative control and Avastin (2.5 mg/mL) as the positive control. Angiogenesis inhibition was quantitatively analyzed using ImageJ software. Micrographs were first converted to 8-bit images, and the threshold was adjusted to optimize vessel visualization. The vascularized area was then measured and normalized relative to the negative control group to determine treatment efficacy.

2.6. Western blotting

Cells were plated in 6-well plates at 4×105 cells/well and treated for 48 hours with either PTX-/Que-loaded Cs NPs or free drug combinations. Following treatment, cells were lysed in buffer containing 50 mM Tris (pH 7.4), 1% Triton X-100, 1% sodium deoxycholate, 0.1% SDS, 150 mM NaCl, 1 mM EDTA, 1 mM Na_3VO_4, and 1 mg/mL leupeptin, supplemented with protease inhibitor cocktail (Roche Applied Science). After protein quantification, equal amounts were separated by 7.5%/12.5% SDS-PAGE under reducing conditions. Samples were denatured in loading buffer at 95°C for 5 minutes before electrophoresis. Proteins were then transferred to nitrocellulose membranes using semi-dry blotting. Membranes were washed three times with 0.05% Tween-20 in PBS (5-minute intervals), blocked with 5% non-fat milk in TBST (20 mM Tris pH 8.0, 150 mM NaCl, 0.05% Tween 20) for 4 hours at room temperature, and probed overnight at 4°C with primary antibodies against TIMP-3 (SC-373839), ZEB1 (SC-515797), and β-actin (SC-517582; Santa Cruz Biotechnology). After incubation with horseradish peroxidase-linked Mouse IgGκ light chain binding protein (SC-516102) for 1 hour at room temperature, protein bands were detected by ECL chemiluminescence (Millipore). Protein expression levels were normalized to β-actin and quantified using Total Lab Quant v12.2 software.

2.7. Investigation of the impact of the prepared formulation on MDA-MB-231 tumor-bearing mice

All animal experiments were meticulously performed in full compliance with the European Union's Directive 2010/63/EU, which establishes standards for the humane care and use of laboratory animals, as well as the ARRIVE (Animal Research: Reporting of In Vivo Experiments) guidelines to ensure transparent and rigorous reporting of animal research. The experimental protocol underwent thorough evaluation and received formal approval from the Laboratory Animal Ethics Committee at Tabriz University of Medical Sciences, Tabriz, Iran, under Approval No. IR.TBZMED.AEC.1402.118, confirming adherence to ethical standards and regulatory requirements for animal welfare. In vivo study was performed using 6–8-week-old female BALB/c nude mice (16-20 g) acquired from the Avicenna Research Institute, Tehran, IRAN to evaluate the antitumor efficacy of Que-/PTX-loaded Cs NPs against MDA-MB-231 breast cancer. Mice were subcutaneously injected with 3×10^5 cells near mammary nipples, and after 7 days when tumors reached ~10 mm diameter, they were divided into three groups (n = 4) receiving: (1) free Que+PTX (0.5 mg/kg Que + 1 mg/kg PTX), (2) equivalent-dose Que-/PTX-Cs NPs, or (3) saline control via daily intraperitoneal injections. Tumor size and body weight were monitored daily until day 7, when SRB-Cs NPs (1 mg/kg) were administered intravenously for fluorescence imaging of tumor volume and biodistribution assessment using a Kodak in vivo imaging system F pro (Carestream Health, Rochester, NY, USA). Mice were then sacrificed for collection of blood, tumors, and major organs (liver, lungs, kidneys, spleen, heart), which were fixed in 10% formalin for H&E staining and histopathological analysis. Tumor growth inhibition percentage (TGI%) was calculated based on relative tumor volume changes, with all procedures approved by Tabriz University of Medical Sciences' Animal Ethics Committee.

$$TGI\% = \frac{(mean\ tumor\ weight\ of\ negative\ control\ mice - tumor\ weight\ of\ treated\ mice)}{men\ tumor\ weight\ of\ negative\ control\ mice}$$

2.8 Statistical analyses

All quantitative results are presented as mean ± SD from a minimum of three independent experimental replicates ($n \geq 3$) to ensure data reproducibility. Statistical analysis was performed using GraphPad Prism (version 9.5.1, San Diego, CA, USA) with one-way ANOVA and Tukey's post-hoc test for multiple comparisons. Statistical significance was set at $p < 0.05$. For multivariate analysis, correlation plots were generated using Microsoft Excel 2021 (Redmond, WA, USA).

3. Results and discussion

3.1 Characterization of prepared NPs

3.1.1. *Size, surface electric charge, morphology and drug-loading efficiency of the prepared nanoparticles*

DLS analysis (Figure 2A) demonstrated mean particle sizes of 82 nm (drug-free), 91.4 nm (Que-loaded), 84.7 nm (PTX-loaded), and 89.1 nm (SRB-loaded) Cs NPs, with corresponding zeta potentials of +23.5, +21.1, +27.6, and +23.5 mV. Visual examination (Figure 2B) confirmed successful NP formation, showing optimal turbidity without precipitation. All formulations displayed narrow size distribution (PDI 0.239-0.341), consistent with the homogeneous particle sizes observed in SEM images (Figure 2D) . The SEM micrographs revealed spherical NPs, with measured sizes smaller than DLS results due to DLS reporting hydrodynamic diameters of hydrated particles, while SEM shows dried particles where water-swollen Cs NPs may shrink. Encapsulation studies showed high efficiency for hydrophobic drugs: ~91% for PTX and ~82% for Que, while the hydrophilic SRB showed lower EE (~50%) but potentially higher drug loading (Figure 2C).

Wang et al. [44] investigated cetuximab-conjugated Cs NPs for Que delivery in PTX-resistant A549 cells, reporting sizes of 291.1 nm (Que-loaded) and 298.4 nm (PTX-loaded) with zeta potentials of +23.6 and +22.3 mV, respectively, though DLS data for unmodified NPs were unavailable. Their PTX EE (~92%) matched our findings, but the larger particle size suggests antibody conjugation or formulation differences may influence characteristics. Notably, their Que-loaded NPs showed significantly lower EE (~13%) compared to our study. Jardim et al. [45] developed Que-loaded Cs NPs (~103 nm, +30 mV) with ~83% EE, aligning with our zeta potential and EE results but exhibiting larger sizes. In summary, our optimized formulations demonstrated superior properties: controlled sizes (82-91 nm), favorable surface charge (+21.1 to +27.6 mV), and high encapsulation efficiencies. A comparison of the characteristics of the drug-loaded Cs NPs prepared in this work and those reported in recent studies is presented in Table 1.

Table 1. Comparative characteristics of similar Cs NP formulations

Formulation	Source	Size	Zeta potential	EE
PTX-loaded Cs NPs	Current study	~85 nm	~28 mV	~91%
Cetuximab-conjugated PTX-loaded Cs NPs	Wang et al. [44]	~298 nm	~22 mV	~92%
Que-loaded Cs NPs	Current study	~91 nm	~21 mV	~82%
Cetuximab-conjugated Que-loaded Cs NPs	Wang et al. [44]	~291 nm	~23 mV	~13%
Que-loaded Cs NPs	Jardim et al. [45]	~103 nm	~30 mV	~83%

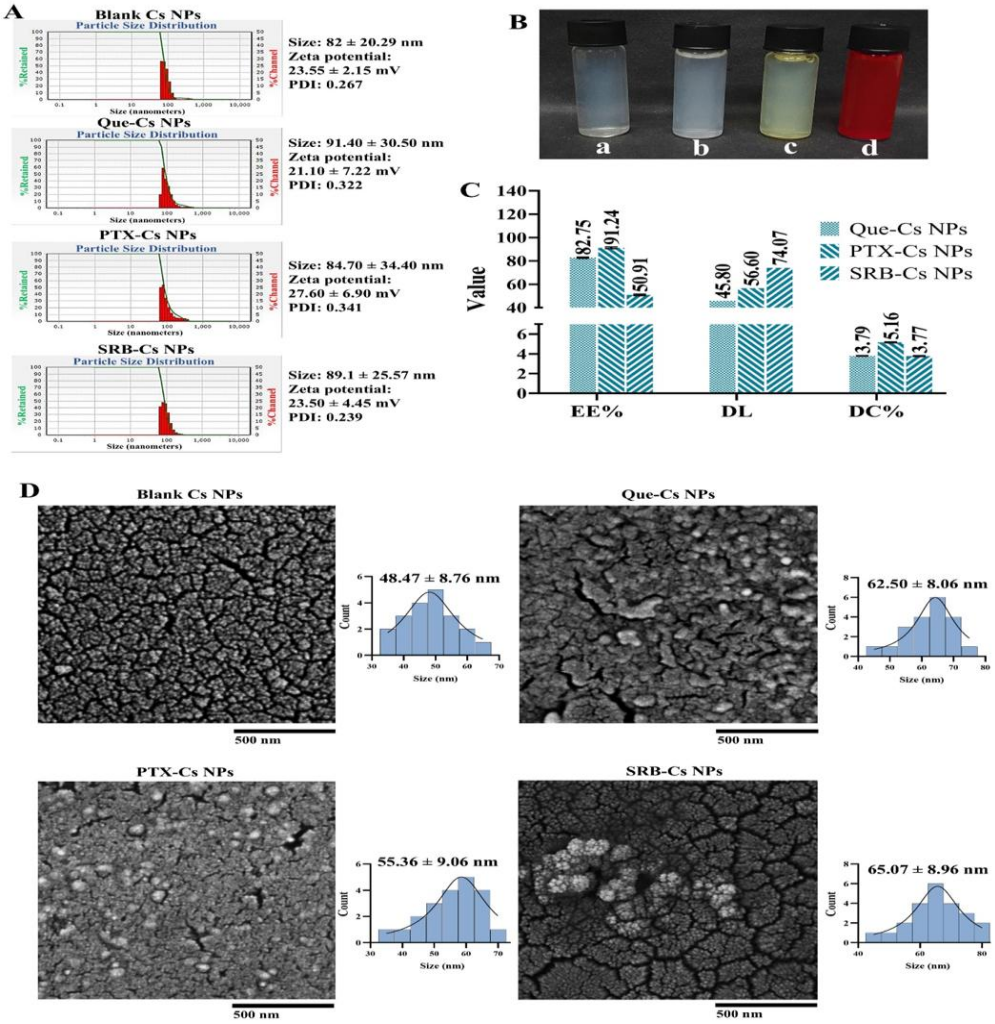

Figure 2. Physicochemical characterization of Cs NPs. (**A**) DLS analysis demonstrating optimal NP properties: hydrodynamic diameter (82-91.4 nm), zeta potential (+21.1 to +27.6 mV), and polydispersity index (PDI: 0.239-0.341). (**B**) Visual appearance of NP suspensions: (**a**) drug-free Cs NPs, (**b**) PTX-loaded, (**c**) Que-loaded, and (**d**) SRB-loaded formulations, all exhibiting stable colloidal dispersions. (**C**) Encapsulation parameters: efficiency (EE%), drug loading (DL), and drug content (DC%) for all formulations. (**D**) SEM micrographs confirming spherical morphology and size uniformity (48.47-65.07 nm)

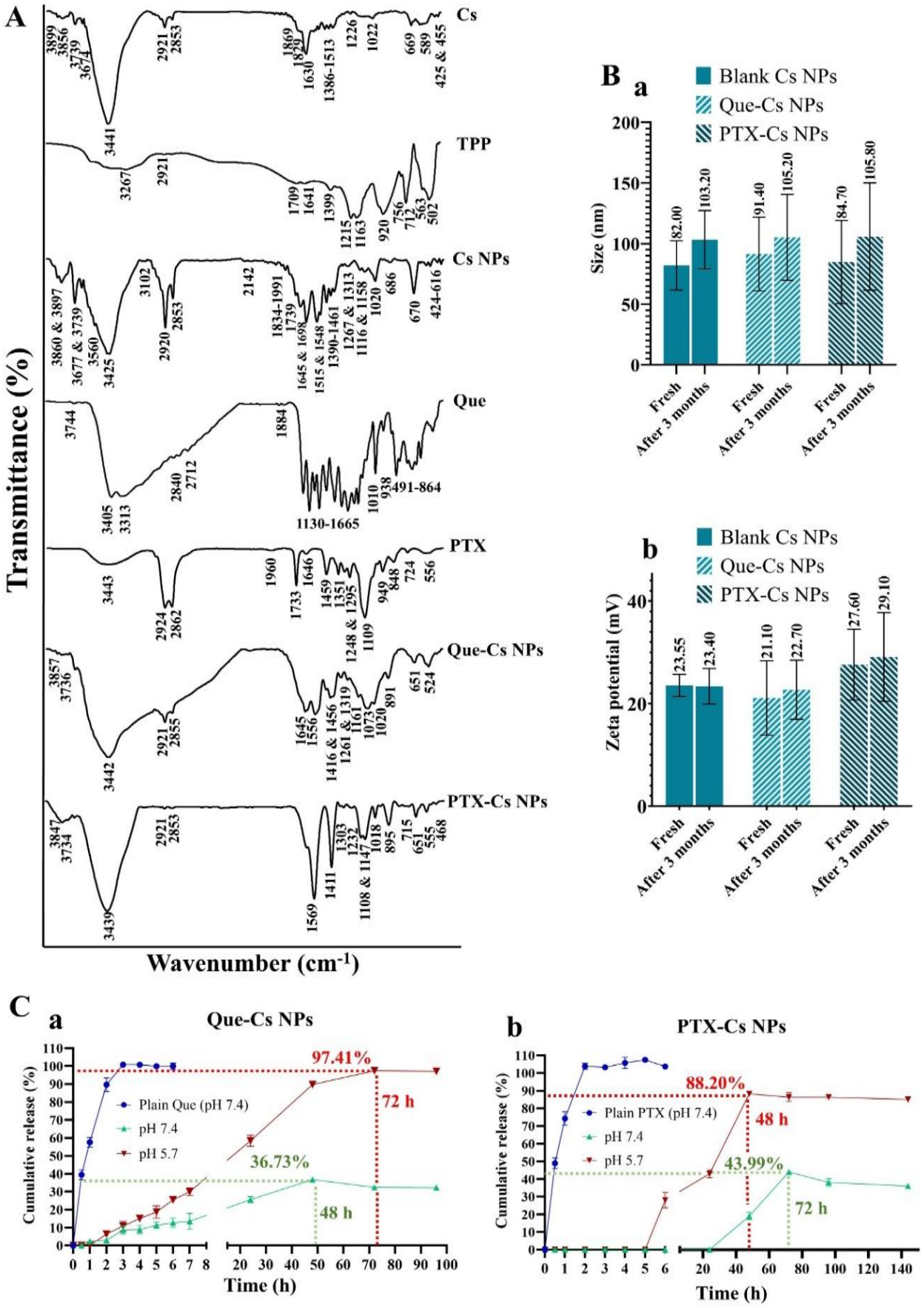

Figure 3. Stability and drug release characterization of Cs NPs. (**A**) FTIR spectra confirming NP formation and successful drug encapsulation for: pure Cs, pure TPP, drug-free Cs NPs, free Que, free PTX, Que-loaded Cs NPs, and PTX-loaded Cs NPs. (**B**) Stability assessment after 3-month storage: (**a**) modest hydrodynamic size increase (Δ~10-20 nm) and (**b**) maintained zeta potential values (±5 mV variation). (**C**) pH-responsive drug release profiles: (**a**) Que-Cs NPs and (**b**) PTX-Cs NPs showing enhanced release at acidic pH (5.7) versus physiological pH (7.4)

3.1.2. *FTIR analysis of prepared NPs*

To investigate the chemical structure and composition of the drugs and drug-free and drug-loaded NPs, samples FTIR analysis was performed to examine the chemical structure and composition of both drug-free and drug-loaded NPs (Figure 3A) . The Cs spectrum displayed characteristic peaks: a broad peak at 3441 cm-1 (O-H/N-H stretching of hydroxyl and amine groups), peaks at 2853/2921 cm-1 (aliphatic C-H stretching of CH2/CH3 groups), peaks between 1513-1630 cm-1 (N-H bending of deacetylated -NH2 groups), and a peak at 1022 cm-1 (C-O stretching of reactive hydroxyl groups), confirming the saccharide structure. The TPP spectrum displayed diagnostic peaks at 920 cm^{-1} (P-O-P bridge), 1163 cm^{-1} (terminal phosphate), and 1215 cm^{-1} (P=O stretch). For Cs NPs, the broader peak at 3425 cm-1 and sharp peak at 1548 cm-1 demonstrated ionic crosslinking with TPP, supported by additional TPP peaks at 1158/1268 cm-1. Que's spectrum revealed polyphenolic characteristics through broad 2900-3400 cm-1 (O-H stretching), 1665 cm-1 (flavone C=O), and 1202 cm-1 (phenolic C-O) peaks. InQue-Cs NPs, enhanced hydrogen bonding was evidenced by peak broadening at 3442 cm-1 (versus Cs NPs) and correlated with reduced zeta potential. PTX exhibited diagnostic peaks at 3443 cm-1 (C7/C2' hydroxyls), 2924/2862 cm-1 (taxane core methylenes), 1733 cm-1 (C13 ester C=O), and 1109 cm-1 (secondary alcohol). For PTX-Cs NPs, the disappearance of PTX's 1733 cm-1 peak and modification of the 3425 cm-1 Cs peak to 3439 cm-1 confirmed drug-polymer interactions, while spectral changes near 1200 cm^{-1} indicated altered ester environments. Notably, although both Cs NPs and PTX show strong C-H stretching vibrations (2800-3000 cm^{-1}), these peaks became significantly attenuated in PTX-Cs NPs, likely resulting from restricted CH_2/CH_3 group mobility due to strong interactions, reflecting both chemical environment changes and PTX entrapment within the Cs NP matrix. These FTIR results not only verified successful NP formation but also explained the high encapsulation efficiencies through observed molecular interactions between drugs and Cs.

3.1.3. *Drug release evaluation*

The drug release profiles of both Que- and PTX-loaded Cs NPs were evaluated at physiological (pH 7.4) and acidic (pH 5.7) conditions, both containing 0.1% (v/v) Tween 80 to enhance drug solubility (Figure 3C) . Both formulations demonstrated enhanced drug release in acidic pH. Specifically, Que-Cs NPs exhibited a gradual release over 48 hours, reaching a plateau with 36.73% cumulative release at pH 7.4, while at pH 5.7, near-complete release (~100%) was achieved by 72 hours. For PTX-Cs NPs, no detectable release occurred during the first 24 hours at physiological pH, followed by a progressive increase to 43.99% by 72 hours. In contrast, acidic conditions triggered detectable PTX release within 5 hours, culminating in 88.2% release by 48 hours before plateauing. These results demonstrate the pH-responsive release behavior of both drugs, potentially advantageous for tumor-targeted delivery given the acidic tumor microenvironment.To elucidate the release mechanisms, various kinetic models (zero-order, first-order, Higuchi, Hixson-Crowell, and Korsmeyer-Peppas) were applied (Figure S2A) . At pH 7.4, Que release followed the Higuchi model (R^2=0.983), indicating diffusion-controlled release through the polymeric matrix. However, at pH 5.7, first-order kinetics (R^2=0.992) predominated, suggesting concentration-dependent release rather than pure diffusion. PTX release at physiological pH best fits the Hixson-Crowell model (R^2=0.909), implying particle degradation or surface area changes over time, possibly due to Cs's temperature sensitivity. In acidic conditions, PTX release adhered to the Korsmeyer-Peppas model (R^2=0.926), signifying a Super Case II transport mechanism [46] .

3.1.4. *Investigation of the stability of Cs NPs*

The stability of the prepared NPs was evaluated after 3 months of storage at 4°C by reanalyzing particle size, zeta potential, and crystalline patterns (Figure 3B) . Results showed a modest size increase of ~10-20 nm in stored NPs, likely due to mild aggregation that could potentially be reversed through ultrasonication. Notably, zeta potential values remained stable with no significant changes observed. Drug leakage during storage was minimal, with Que-Cs NPs showing 2.39% drug loss and PTX-Cs NPs demonstrating only 0.22% leakage. XRD analysis (Figure S1) revealed that drug-free Cs NPs and Que-Cs NPs maintained similar crystalline patterns after storage. However, while the characteristic peaks of freshly prepared PTX-Cs NPs persisted post-storage, two new peaks emerged, possibly indicating crystallization of the small fraction of leaked hydrophobic PTX [47] .

3.2. In vitro investigation of cellular uptake and anticancer effects of Que-/ PTX-Cs NPs on MDA-MB-231 cells

3.2.1. *Cellular uptake evaluation*

The cellular uptake efficiency of Cs NPs was evaluated using SRB as a fluorescent marker [48] . Flow cytometry analysis (Figure 4A) demonstrated that Cs NPs significantly enhanced SRB internalization compared to free SRB. After 1 hour of treatment, cellular uptake increased from 9.75% (free SRB) to 51.73% (SRB-loaded Cs NPs). This enhancement became more pronounced after 4 hours, with uptake reaching 24.83% for free SRB and

96.85% for SRB-Cs NPs. Fluorescence microscopy images (Figure 4B) further confirmed these findings, clearly showing substantially higher intracellular fluorescence intensity for NP-treated cells, in excellent agreement with the quantitative flow cytometry data.

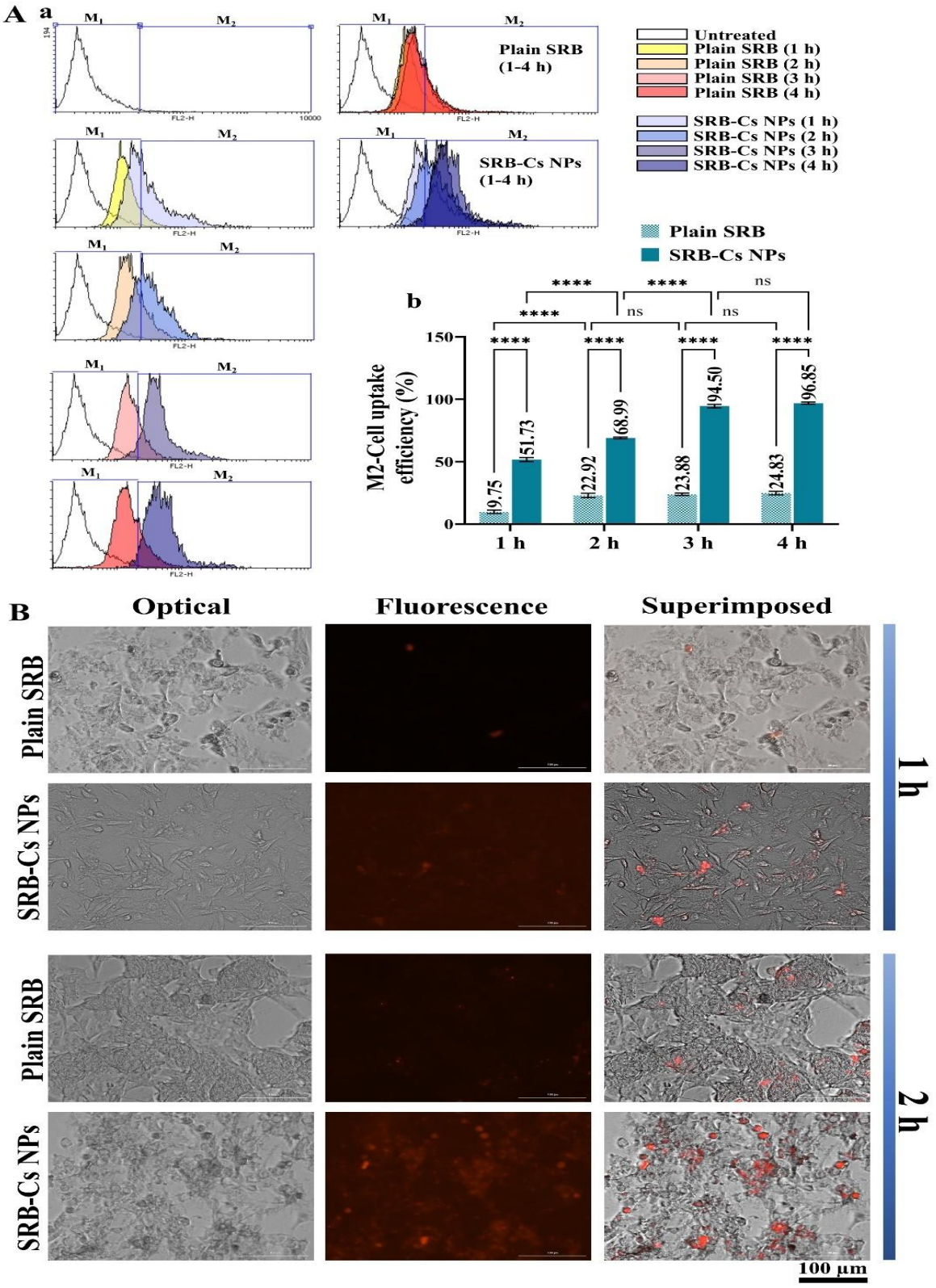

Figure 4. Cellular uptake evaluation of SRB-loaded Cs NPs (SRB-Cs NPs). (**A**) Flow cytometry analysis: (**a**) representative histograms and (**b**) quantitative time-course data demonstrating significantly enhanced cellular internalization of SRB-Cs NPs compared to free SRB. Additionally, NP formulations exhibited time-dependent uptake increase. Fluorescence microscopy images (**B**) corroborated these findings, revealing high intracellular fluorescence in SRB-Cs NP-treated cells versus minimal signal in free SRB controls. ns: $p > 0.05$, ****: $p < 0.0001$

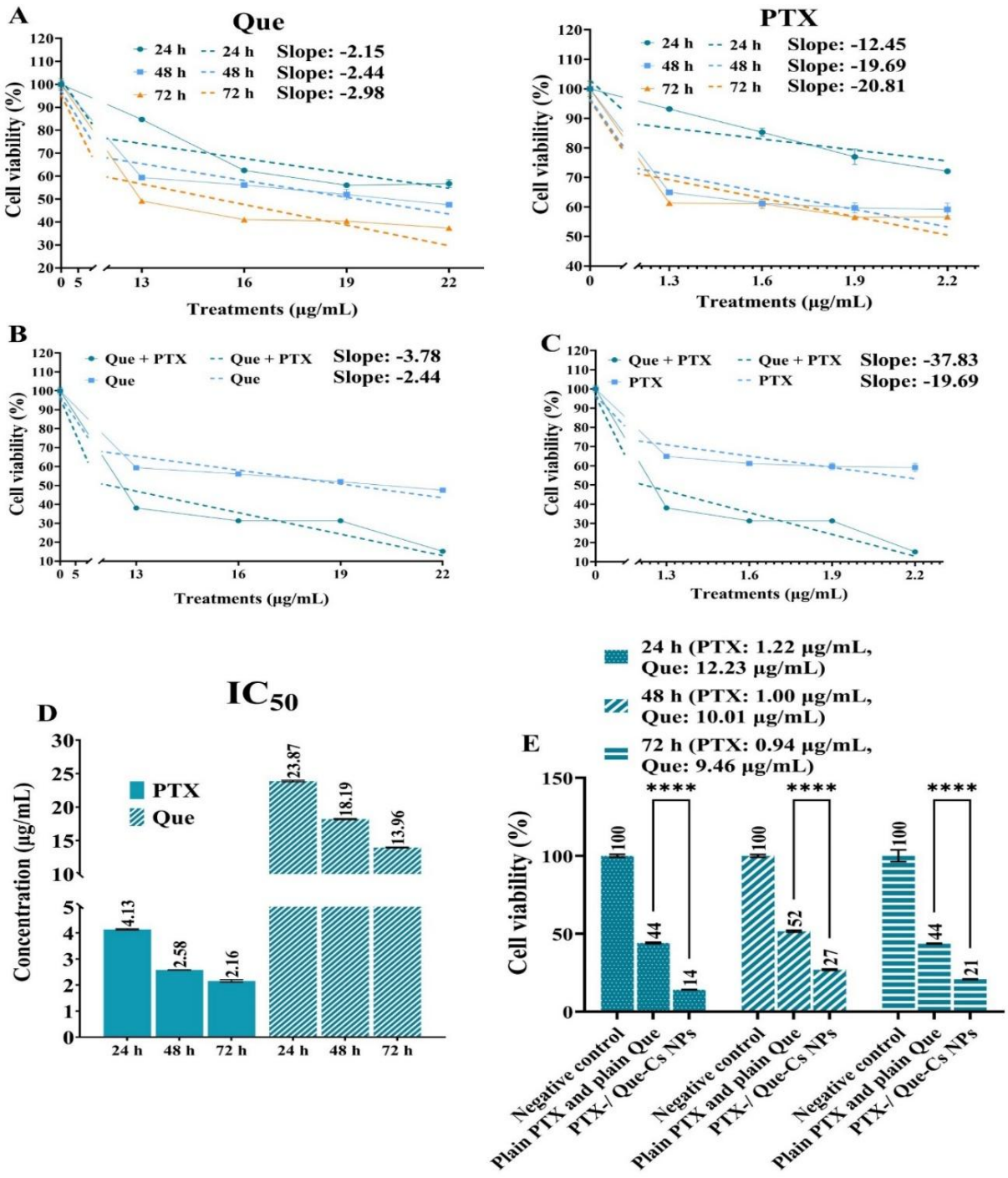

Figure 5. Cytotoxicity assessment of free drugs and NP formulations in MDA-MB-231 cells (MTT assay). (A) Time- and concentration-dependent cytotoxicity of single-agent treatments. (B-C) Enhanced therapeutic efficacy of the 1:10 PTX:Que combination compared to individual drugs at equivalent concentrations. (D) IC50 values demonstrating progressive potency increase: Que (4.13-2.16 µg/mL) and PTX (23.87-13.96 µg/mL) from 24-72h. (E) Superior cytotoxicity of Que-/PTX-Cs NPs versus free drug combination at Fa50 concentrations (****: $p < 0.0001$), as calculated by CompuSyn software

Table 2. Effects of Que+PTX and Que-/PTX-Cs NPs on apoptosis, necrosis, and nuclear area in MDA-MB-231 cells

	Negative control	Que + PTX	Que-Cs NPs + PTX-Cs NPs
Healthy cells (%)	98.55 ± 0.20	47.09 ± 3.24	5.35 ± 0.70
Necrosis (%)	0.31 ± 0.10	4.34 ± 1.07	1.79 ± 0.02
Early apoptosis (%)	0.39 ± 0.02	11.03 ± 1.26	1.13 ± 0.19
Late apoptosis (%)	0.73 ± 0.12	37.52 ± 3.43	91.72 ± 0.91
Nuclear area (%)	100 ± 24.17	76.67 ± 21.23	41.67 ± 18.38

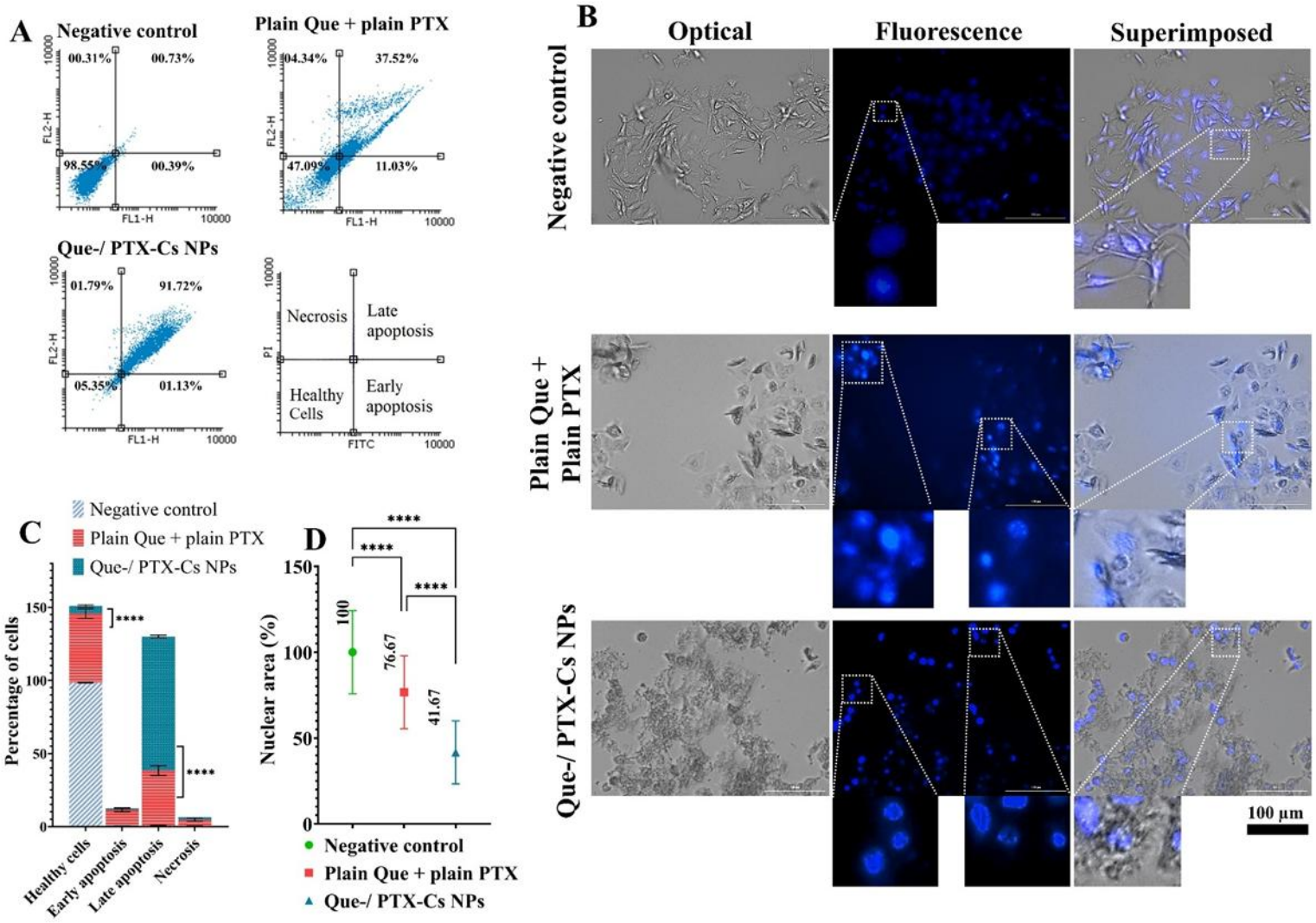

Figure 6. Apoptosis induction and nuclear morphological changes in MDA-MB-231 cells. (A) Flow cytometry dot plots of annexin V-FITC/PI staining with (C) corresponding quantification demonstrating that Que-/PTX-Cs NPs significantly enhanced late apoptosis (91.72% vs 37.52% in free drug combination) while reducing viable cell populations (5.35% vs 47.09%). (B) DAPI staining qualitative analysis revealed distinct nuclear phenotypes: free drug combination primarily induced nuclear condensation (early apoptosis), whereas Que-/PTX-Cs NPs caused extensive fragmentation (late apoptosis/necrosis) with complete cellular disruption. (D) Semi-quantitative morphometric analysis confirmed nuclear area reduction by 23.3% (free drugs) and 58.3% (NPs), corroborating the stage-specific apoptotic effects. ****: $p < 0.0001$

3.2.2. *Evaluation of cytotoxicity using MTT assay*

MTT assay results demonstrated time-dependent cytotoxic effects for both Que and PTX, as confirmed by linear regression analysis (Figure 5A) . The calculated IC50 values decreased progressively with longer exposure times: for Que, values were 4.13, 2.58, and 2.16 µg/mL at 24, 48, and 72 hours, respectively, while PTX showed higher IC50 values of 23.87, 18.19, and 13.96 µg/mL at the same time points (Figure 5D) .

Combination therapy with Que and PTX (Figure S2C) exhibited enhanced cytotoxicity compared to single-agent treatments. Comparative analysis at 48 hours (Figures 5B & C) revealed dose-responsive and significant improvement in anticancer effects with the combined treatment. Moreover, the MTT assay also revealed that the prepared blank Cs NPs are non-cytotoxic and even promote cell proliferation (Figure S2B) . This indicates that the potent cytotoxicity of the drug-loaded Cs NPs is caused by the drug itself, not by carrier toxicity. CompuSyn analysis quantified these interactions. At 24 hours, the Fa50 concentrations were 1.22 µg/mL for PTX and 12.23 µg/mL for Que, with a combination index (CI) of 1.0, indicating additive effects.

By 48 hours, the Fa50 decreased to 1 µg/mL (PTX) and 10.01 µg/mL (Que) with a CI of 0.6, demonstrating synergy. At 72 hours, further synergy was observed (CI = 0.9) with Fa50 values of 0.94 µg/mL (PTX) and 9.46 µg/mL (Que). Notably, drug-loaded Cs NPs (using Fa50 concentrations from free drugs) significantly enhanced cytotoxicity compared to free drug combinations (Figure 5E) . The 48-hour Fa50 concentrations were selected for subsequent biological assays due to their optimal synergistic profile.

3.2.3. *Investigation of the impact of the drug-loaded Cs NPs on apoptosis induction and nuclear morphology alterations*

Flow cytometry analysis of annexin-V-FITC/PI-stained MDA-MB-231 cells revealed distinct cell death patterns following different treatments (Figure 6A) . The free drug combination (Que+PTX) induced 4.34% necrosis, 11.03% early apoptosis, and 37.52% late apoptosis, with 47.09% viable cells remaining. In contrast, Que-/PTX-loaded Cs NPs demonstrated markedly enhanced efficacy, showing only 1.79% necrosis, 1.13% early apoptosis, but 91.72% late apoptosis, with merely 5.35% viable cells (Figure 6C) . These results indicate that NP-mediated delivery not only increases total cell death but also specifically promotes late-stage apoptosis. DAPI staining micrographs (Figure 6B) corroborated these findings: while free drugs primarily caused nuclear condensation (early apoptosis) with minor fragmentation (late apoptosis), as well as noticeable alterations in overall cell morphology. In contrast, NP treatment induced extensive nuclear fragmentation and complete disruption of cellular architecture. Quantitative analysis showed the free drug combination reduced nuclear area by 23.3%, whereas Que-/PTX-Cs NPs caused a 58.3% reduction (Figure 6D) . Table 2 summarizes these treatment effects on apoptosis induction and nuclear alterations in tumor cells.

3.2.4. *Effect of Que-/ PTX-Cs NPs on 3D-cultured MDA-MB-231 mammospheres*

The therapeutic efficacy of various treatments was evaluated using MDA-MB-231 mammospheres (Figure 7). While PTX treatment showed minimal impact on mammosphere density (comparable to negative control), PTX-loaded Cs NPs demonstrated slightly greater effects, though both exhibited the weakest density reduction among all treatments. Que treatments (both free and NP-loaded) showed superior efficacy compared to the free drug combination, possibly due to acquired resistance in 3D-cultured cells. Notably, the combined Que-/PTX-Cs NP treatment outperformed all other groups, achieving most significant density reduction. SEM analysis (Figure 7B) revealed distinct morphological changes: negative control mammospheres maintained compact structures with smooth surfaces, while treated groups showed disintegration and surface roughness. Multiple regression analysis (Figure 7D) of both density and size parameters provided further insights. PTX treatment (1 µg/mL) failed to inhibit mammosphere growth (size changes similar to the negative control). Although Que and Que-Cs NPs showed comparable size reduction patterns, the NP formulation more effectively reduced density, possibly by compromising cellular protective functions. Interestingly, combination therapies (both free drugs and PTX-Cs NPs) affected diameter more than density, likely due to apoptotic/necrotic debris accumulation. The Que-/PTX-Cs NP combination uniquely reduced both diameter and density, correlating with apoptosis/necrosis assays and SEM observations, confirming its potent dual action on cell viability and structural integrity.

3.2.5. *Evaluation of cell migration inhibition*

A migration assay was performed on 2D-cultured MDA-MB-231 cells to evaluate treatment effects (Figure 8) . The Que-/PTX-Cs NP combination demonstrated the strongest anti-migratory activity (99.98% inhibition), whereas free Que showed negligible impact (5.45% vs negative control). Que-Cs NPs and the free drug combination exhibited comparable migration inhibition. Both PTX and PTX-Cs NPs displayed similar efficacy until 48 hours; however, by 72 hours, PTX-treated cells regained migration capacity, reaching levels observed with the free drug combination. Notably, the free drug combination underperformed relative to expectations, consistent with mammosphere study findings. To differentiate between cytotoxicity and direct anti-migratory effects, both cell coverage and migration distance were analyzed using multiple regression (Figure 8C) . Negative controls showed progressive increases in both parameters. While Que reduced cell coverage without affecting migration (suggesting concentration-dependent activity), PTX-Cs NPs and the free drug combination exhibited parallel reductions in coverage and migration, implying cytotoxicity-driven effects. Conversely, Que-Cs NPs, PTX-Cs NPs, and the Que-/PTX-Cs NP combination disproportionately suppressed migration relative to coverage reduction, indicating potential direct interference with migratory machinery.

3.2.6. *Effect of Que-/ PTX-Cs NPs on angiogenesis suppression*

The CAM assay served as an effective in vivo model for evaluating the anti-angiogenic potential of tested compounds. Results demonstrated that both the Que-PTX combination and Que-/PTX-loaded Cs NPs significantly inhibited angiogenesis (Figure 9A) . Quantitative analysis revealed a 44.96% increase in vascularization for negative controls over 48 hours, while treatment groups showed substantial suppression: 50.37% inhibition for free drug combination and 93.94% for NP-formulated drugs (Figure 9Ab). These findings, when considered alongside migration assay results, highlight the dual therapeutic advantage of these treatments, simultaneously targeting both angiogenic processes and cell motility. The observed anti-angiogenic effects, combined with direct cytotoxic activity, suggest a comprehensive mechanism for tumor growth inhibition [49] .

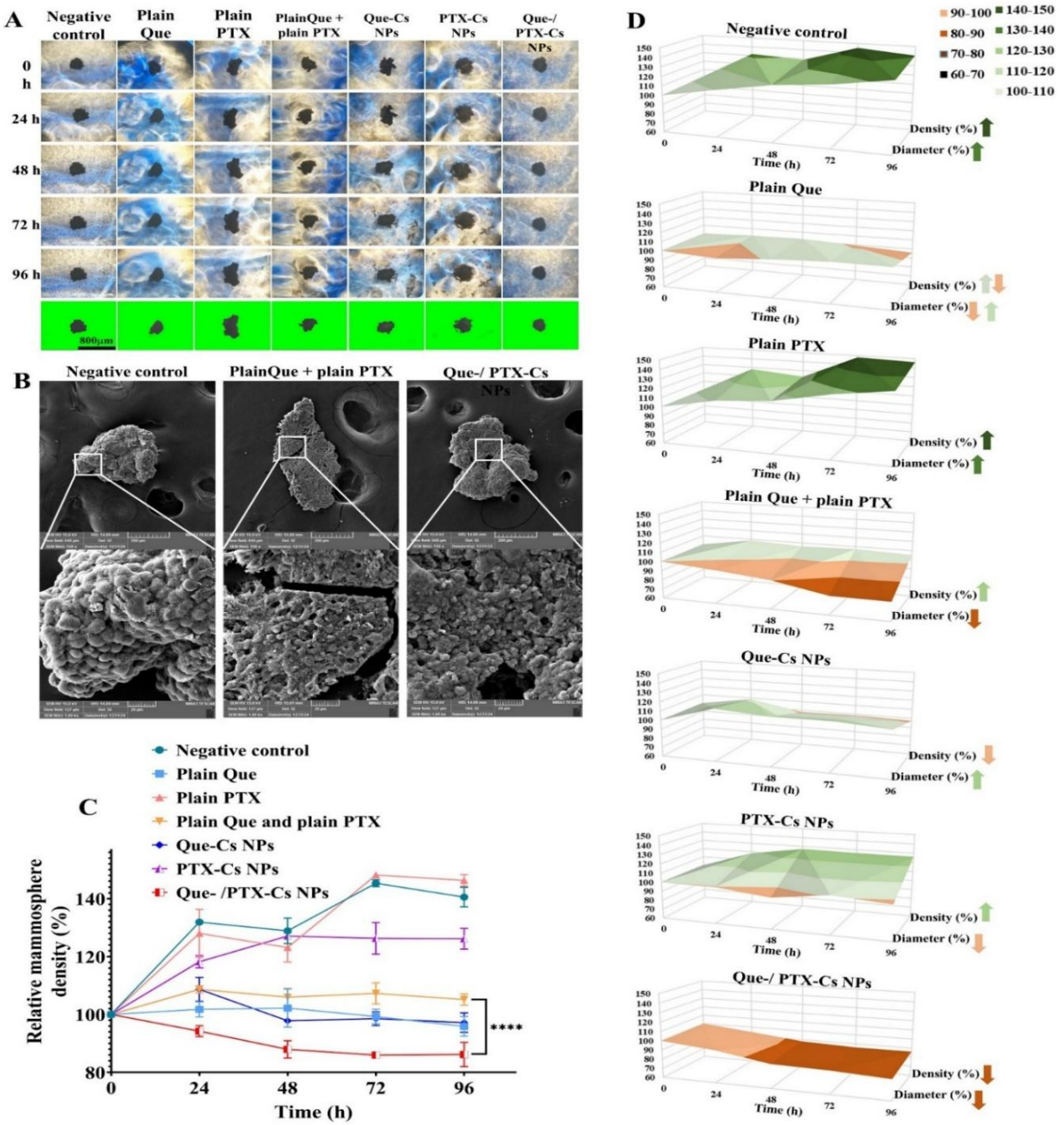

Figure 7. Therapeutic effects on MDA-MB-231 mammospheres. (A) Bright-field micrographs and (C) quantitative density analysis demonstrating superior efficacy of Que-/PTX-Cs NPs versus free drug combinations. (B) SEM characterization revealing structural disintegration in treated mammospheres: free drug- and NP-treated groups exhibited rough surfaces and reduced cell size compared to smooth, compact negative controls. (D) Multivariate regression plots correlating temporal changes in mammosphere diameter and density, highlighting treatment-specific disruption patterns. ****: $p < 0.0001$

3.2.7. *Evaluation of TIMP-3 and ZEB1 expression using western blotting*

TIMP-3 and ZEB1 represent critical regulatory proteins in cancer progression, with opposing roles in tumor behavior. TIMP-3 functions as an MMP inhibitor that suppresses cell migration and is characteristically downregulated in malignancies. Conversely, ZEB1 promotes tumor invasiveness and angiogenesis, potentially serving as a molecular bridge between metastatic potential and vascular development. Western blot analysis (Figure 9B) demonstrated that both combination therapies significantly modulated these proteins: the Que+PTX combination downregulated ZEB1 by 1.19-fold and upregulated TIMP-3 by 1.24-fold, while Que-/PTX-Cs NPs showed more pronounced effects (1.85-fold ZEB1 reduction and 1.26-fold TIMP-3 elevation). These molecular alterations correlate strongly with functional assays, where NP-mediated treatment exhibited superior anti-migratory and anti-angiogenic activity, collectively indicating its potent suppression of invasive tumor behavior.

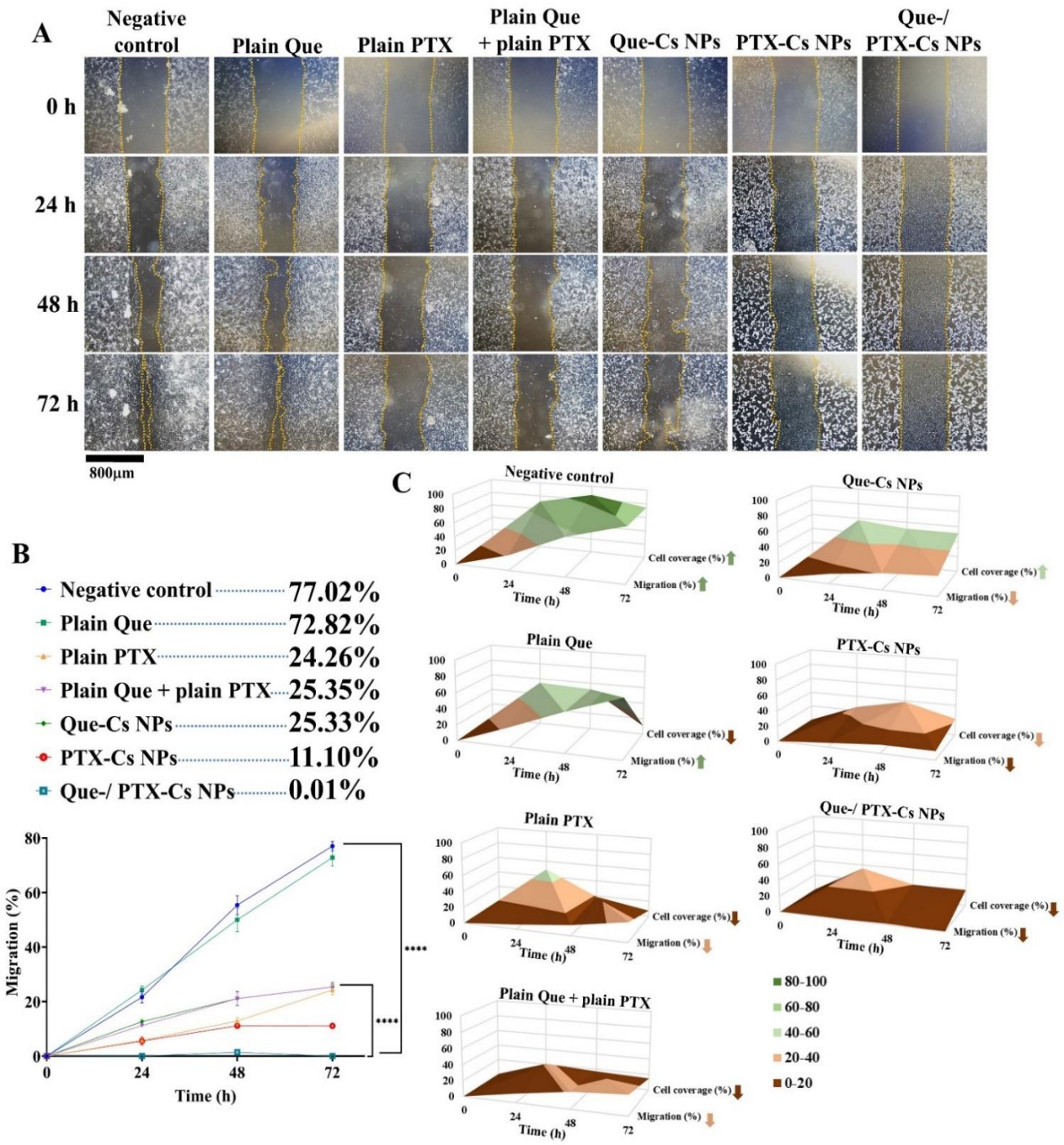

Figure 8. Anti-migratory effects on MDA-MB-231 cells. (**A**) Representative migration assay images and (**B**) quantitative analysis demonstrating that Que-/PTX-Cs NPs achieved near-complete inhibition (99.98%) of cell migration compared to the free drug combination (67.08% inhibition) at 72 h post-treatment. (**C**) Multivariate regression analysis of cell coverage versus migration distance, distinguishing direct anti-migratory effects from cytotoxicity-mediated inhibition. ****: $p < 0.0001$

3.3. Evaluation of anti-cancer efficiency of Que-/ PTX-Cs NPs on MDA-MB-231tumors in vivo

MDA-MB-231 tumor-bearing BALB/c nude mice were used to evaluate the therapeutic potential of combination therapies (Figure 10) . While both free drug combination (Que+PTX) and Que-/PTX-loaded Cs NPs reduced tumor volume compared to negative controls, only the NP formulation showed statistically significant effects. The Que-/PTX-Cs NP treatment dramatically decreased the tumor growth slope from 133.3 (saline group) to 14.69. Rapid tumor progression in all groups led to corresponding increases in body weight. In vivo imaging revealed 12.83% and 66.29% tumor volume reduction for free drugs and NP treatments, respectively, with TGI rates of 41.45% and 71.79% (Figures 10B, G, H). Biodistribution studies demonstrated targeted accumulation, with 64.27% of injected NPs localizing in tumors, followed by lungs (23.89%), liver (9.84%), and kidneys (2%) (Figures 10C, I). The elevated pulmonary uptake may reflect both normal

Cs NP distribution patterns[50] and potential metastatic involvement, as suggested by subsequent findings. Tumor morphology analysis showed vascularized, hemorrhagic lesions in negative controls (Figure 10D), contrasting with their appearance pre-injection (Figure S4A). Necropsy revealed extensive metastatic spread in untreated mice, characterized by dark tumor foci throughout the body (Figure S4B), while both treatment groups showed a marked reduction in metastatic burden.

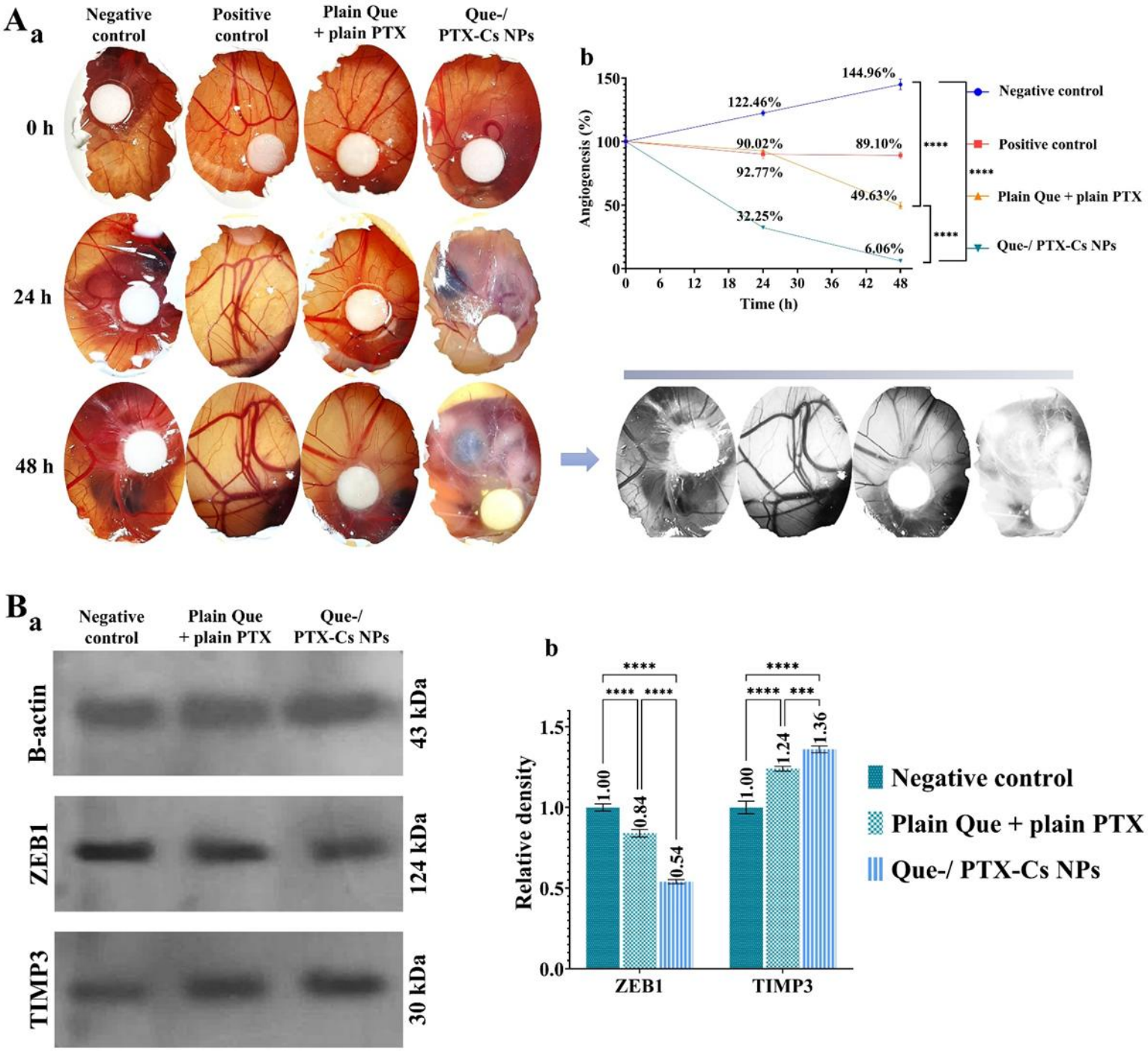

Figure 9. Anti-angiogenic and molecular effects of combination therapies. (A) CAM assay results: (a) Representative images and (b) quantitative analysis showing 50.37% (free drug combination) and 93.94% (Que-/PTX-Cs NPs) angiogenesis inhibition versus negative control. (B) Western blot analysis: (a) Protein expression profiles and (b) densitometric quantification demonstrating significant ZEB1 downregulation (1.85-fold) and TIMP-3 upregulation (1.26-fold) with Que-/PTX-Cs NPs, exceeding free drug effects (1.19-fold ZEB1 reduction, 1.24-fold TIMP-3 increase). ***: $p < 0.001$, ****: $p < 0.0001$

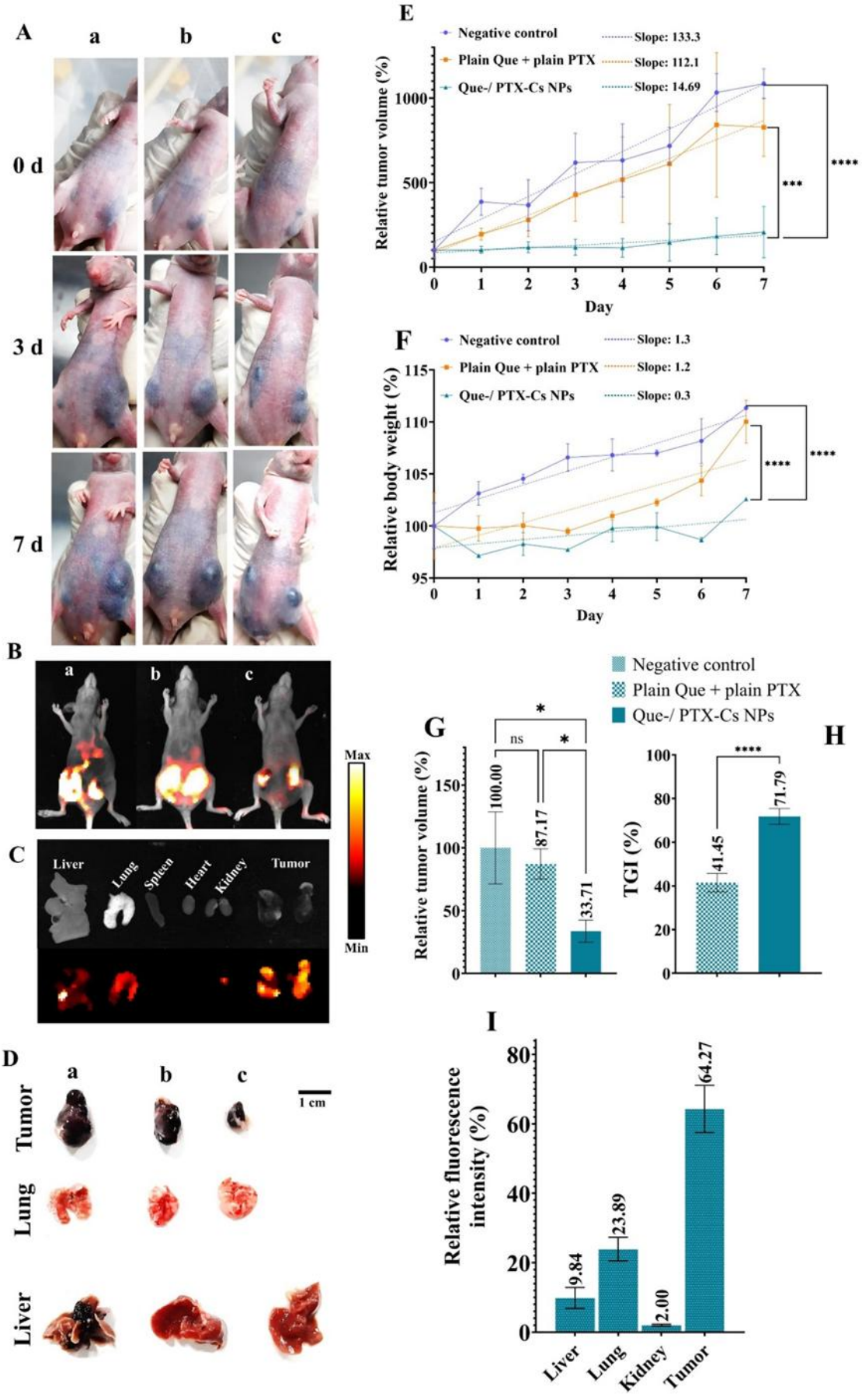

Figure 10. *In vivo* therapeutic efficacy in MDA-MB-231 xenograft models. (**A**) Representative photographs and (**E**) tumor growth curves demonstrate significant tumor volume reduction with Que-/PTX-Cs NPs versus the free drug combination. (**B**, **G**) *In vivo* imaging confirmed enhanced antitumor effects (71.79% TGI) with NP treatment after 7 days (vs 41.45% for free drugs) (**H**). (**F**) Body weight monitoring revealed that all of the studied mice showed moderate weight gain. (**C**, **I**) Biodistribution analysis showed passively-targeted accumulation: 64.27% (tumors), 23.89% (lungs), 9.84% (liver), and 2% (kidneys). (**D**) Gross morphology of resected organs: (**a**) negative controls exhibited large tumors and metastatic liver involvement, (**b**) free drug combination showed intermediate improvement, while (**c**) Que-/PTX-Cs NPs demonstrated the smallest tumors and near-normal liver/lung morphology. ns: $p > 0.05$, *: $p < 0.05$, ***: $p < 0.001$, ****: $p < 0.0001$

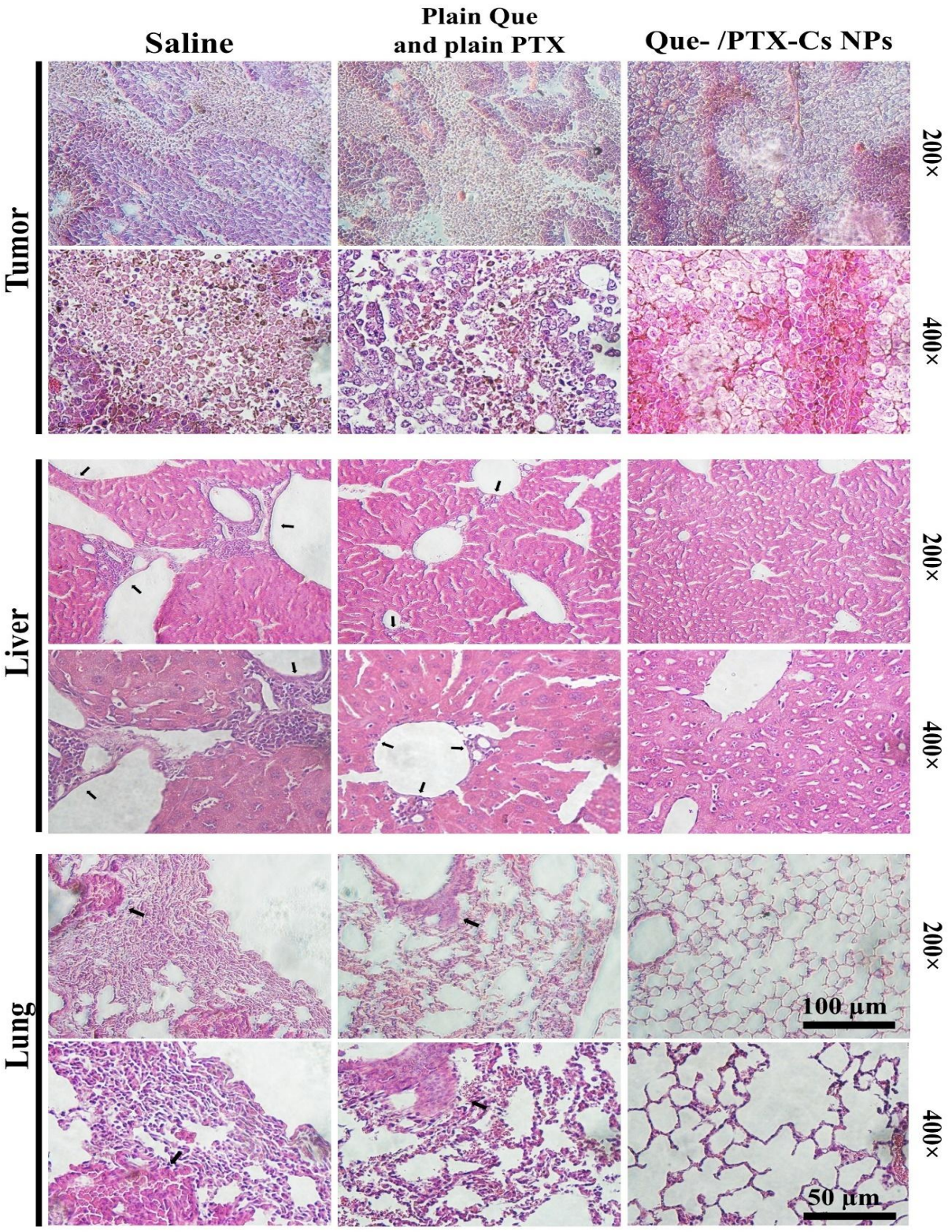

Figure 11. Histopathological analysis of H&E-stained tissues from xenograft models. (**A**) Tumor sections: Negative control and free drug-treated groups exhibited heterogeneous invasive carcinoma morphology, while Que-/PTX-Cs NP treatment showed more uniform tissue architecture with increased anucleate zones. (**B**) Liver and lung sections: Prominent pleomorphic cell infiltrates (black arrows) in negative controls and free drug groups were markedly reduced in NP-treated mice. (**C**) Pulmonary evaluation: Only Que-/PTX-Cs NPs restored near-normal alveolar structure, with minimal pleomorphic cells observed

4. Challenges and future direction

Here, Que-/PTX-Cs NPs were developed, and the combination therapy's antitumor, antimigratory, and antiangiogenic effects were evaluated. In vitro and in vivo data show strong potential for TNBC suppression, yet several hurdles remain for clinical translation. A primary concern is the formulation's long-term stability, which needs to be studied and enhanced. Additionally, the current

lab-scale NP synthesis methods present scaling-up difficulties. These processes must be adapted or replaced to achieve mass production of drug-loaded NPs with consistent properties and minimal variation. Although Cs is considered biocompatible, detailed immunogenicity studies are essential to verify its in vivo safety. Addressing these points is critical for developing standardized, repeatable, sterile, and safe drug-loaded Cs NPs for clinical use. While patient-derived models are a viable next step, future research should also focus on optimizing the NP formulations for pharmacokinetic studies in larger animal models. A deeper exploration of the molecular interactions between ZEB1, TIMP-3, and other EMT-related factors (e.g., E-cadherin, Snail, MMP2, MMP9) could clarify the anti-metastatic mechanisms. The efficacy against resistant TNBC subtypes might be improved by combining Que-/PTX-Cs NPs with immunotherapies like PD-1/PD-L1 inhibitors or other targeted drugs, thereby simultaneously addressing EMT and immune evasion. Another promising avenue is combining this NP platform with oligonucleotide therapy to target alternative key survival pathways in malignant neoplasms.

5. Conclusion and future remarks

This study establishes the remarkable therapeutic potential of Que-/PTX-Cs NPs as a transformative nanoplatform for combating aggressive MDA-MB-231 triple-negative breast cancer (TNBC), with a particular focus on suppressing epithelial-mesenchymal transition (EMT), a critical driver of metastasis. Characterized by sizes of 82–91.4 nm, zeta potentials of +21.1 to +27.6 mV, and encapsulation efficiencies exceeding 80%, these NPs demonstrated potent anti-tumor, anti-metastatic, and anti-angiogenic effects in both in vitro and in vivo models. In vitro, Que-/PTX-Cs NPs induced 91.72% late apoptosis, achieved near-complete (99.98%) inhibition of cell migration, and significantly curtailed mammosphere formation in 3D cultures, effectively disrupting EMT-mediated invasiveness. These effects were driven by the NPs' ability in regulating key EMT modulators: ZEB1, a transcription factor that promotes EMT by suppressing E-cadherin and enhancing mesenchymal traits, was downregulated by 1.85-fold, while TIMP-3, an inhibitor of matrix metalloproteinases (MMPs) critical for extracellular matrix degradation during EMT, was upregulated by 1.26-fold. The near-complete inhibition of cell migration, as evidenced by the scratch assay, underscores the NPs' capacity to block EMT-driven invasiveness, with Que-/PTX-Cs NPs outperforming free drug combinations. Furthermore, a 93.94% reduction in angiogenesis in the chorioallantoic membrane (CAM) assay highlights their ability to disrupt vascular networks essential for metastatic dissemination, potentially through. ZEB1's regulatory links to angiogenesis-related genes such as Hif-1α and VEGFB. In vivo, BALB/c nude mice bearing MDA-MB-231 xenografts treated with Que-/PTX-Cs NPs exhibited 71.79% tumor growth inhibition and significantly reduced metastatic spread, particularly in the liver and lungs, with 64.27% NP accumulation in tumors and no systemic toxicity. These in vivo outcomes further validate the NPs' anti-EMT efficacy, as the reduction in metastatic foci reflects their ability to suppress the EMT-driven metastatic cascade. The synergistic action of Que, with its anti-metastatic and antioxidant properties, and PTX, a potent chemotherapeutic, delivered via Cs NPs, overcomes their individual pharmacokinetic limitations, amplifying both anti-EMT and anti-tumor effects. Collectively, these findings position Que-/PTX-Cs NPs as a highly promising therapeutic strategy for TNBC, addressing tumor growth, EMT-driven metastasis, and angiogenesis through a single delivery system. Future research should prioritize optimizing these NP formulations for clinical translation, focusing on scalability, long-term stability, and pharmacokinetic profiling in larger animal models. Further exploration of the molecular interplay between ZEB1, TIMP-3, and other EMT-related pathways could deepen understanding of their anti-metastatic mechanisms. Combining Que-/PTX-Cs NPs with immunotherapies may enhance efficacy against resistant TNBC subtypes by simultaneously targeting EMT and immune evasion. Clinical trials are essential to evaluate safety, dosing, and therapeutic outcomes in human TNBC patients, paving the way for personalized nanomedicine to address this challenging malignancy.

Authors Contribution

All authors reviewed the manuscript. Hamed Dadashi: Investigation, Writing – original draft. Amir Reza Nazemiyeh: Investigation, Formal analyses. Niloofar Ahdeno: Investigation. Parnia Kehtari: Investigation. Samar Mahari: Investigation. Yadollah Omidi: Validation, Writing – review & editing, Somayeh Vandghanooni: Supervision, Writing – review & editing. Morteza Eskandani: Conceptualization, Supervision, Writing – review & editing.

Declaration of competing interest

The authors declare that they have no known competing interests.

Acknowledgments

This research was funded by Tabriz University of Medical Sciences, Tabriz, Iran (Grant No. 73091).

Ethics Approval

The experimental protocol underwent thorough evaluation and received formal approval from the Laboratory Animal Ethics Committee at Tabriz University of Medical Sciences, Tabriz, Iran, under Approval No. IR.TBZMED.AEC.1402.118. This approval confirms

adherence to ethical standards and regulatory requirements for animal welfare.

References

[1] Smolarz, B., Nowak, A. Z., Romanowicz, H., Breast cancer—epidemiology, classification, pathogenesis and treatment (review of literature). Cancers 14, 2569 (2022).

[2] Xiong, X., Zheng, L.-W., Ding, Y., Chen, Y.-F., Cai, Y.-W., Wang, L.-P., Huang, L., Liu, C.-C., Shao, Z.-M., Yu, K.-D., Breast cancer: pathogenesis and treatments. Signal Transduct Target Ther 10, 49 (2025).

[3] Taskindoust, M., Thomas, S. M., Sammons, S. L., Fayanju, O. M., DiLalla, G., Hwang, E. S., Plichta, J. K., Survival outcomes among patients with metastatic breast cancer: review of 47,000 patients. Ann Surg Oncol 28, 7441-7449 (2021).

[4] Riggio, A. I., Varley, K. E., Welm, A. L., The lingering mysteries of metastatic recurrence in breast cancer. Br J Cancer 124, 13-26 (2021).

[5] Narezkina, A., Narayan, H. K., Zemljic-Harpf, A. E., Molecular mechanisms of anthracycline cardiovascular toxicity. Clinical Science 135, 1311-1332 (2021).

[6] Torri, G. B., Soldatelli, M. D., Luersen, G. F., Almeida Ghezzi, C. L., Imaging of chemotherapy-induced liver toxicity: an illustrated overview. Hepatic Oncology 8, HEP32 (2021).

[7] Gupta, S., Portales-Castillo, I., Daher, A., Kitchlu, A., Conventional chemotherapy nephrotoxicity. Adv Chronic Kidney Dis 28, 402-414. e1 (2021).

[8] Eskandani, R., Kazempour, M., Farahzadi, R., Sanaat, Z., Eskandani, M., Adibkia, K., Vandghanooni, S., Mokhtarzadeh, A., Engineered nanoparticles as emerging gene/drug delivery systems targeting the nuclear factor-κB protein and related signaling pathways in cancer. Biomed Pharmacother 156, 113932 (2022).

[9] Hosseini, S. M., Mohammadnejad, J., Najafi-Taher, R., Zadeh, Z. B., Tanhaei, M., Ramakrishna, S., Multifunctional carbon-based nanoparticles: Theranostic applications in cancer therapy and diagnosis. ACS Applied Bio Materials 6, 1323-1338 (2023).

[10] Khursheed, R., Dua, K., Vishwas, S., Gulati, M., Jha, N. K., Aldhafeeri, G. M., Alanazi, F. G., Goh, B. H., Gupta, G., Paudel, K. R., Biomedical applications of metallic nanoparticles in cancer: Current status and future perspectives. Biomed Pharmacother 150, 112951 (2022).

[11] Mirzaee Rad, F., Tafvizi, F., Noorbazargan, H., Iranbakhsh, A., Ag-doped ZnO nanoparticles synthesized through green method using Artemisia turcomanica extract induce cytotoxicity and apoptotic activities against AGS cancer cells: an in vitro study. J Nanostruct Chem 14, 403-418 (2024).

[12] Ghanbarikondori, P., Aliakbari, R. B. S., Saberian, E., Jenča, A., Petrášová, A., Jenčová, J., Khayavi, A. A., Enhancing cisplatin delivery via liposomal nanoparticles for oral cancer treatment. Indian J Clin Biochem 40, 211-217 (2024).

[13] Rasouliyan, F., Eskandani, M., Jaymand, M., Akbari Nakhjavani, S., Farahzadi, R., Vandghanooni, S., Eskandani, M., Preparation, physicochemical characterization, and anti-proliferative properties of Lawsone-loaded solid lipid nanoparticles. Chemistry and Physics of Lipids 239, 105123 (2021).

[14] Vandghanooni, S., Rasoulian, F., Eskandani, M., Akbari Nakhjavani, S., Eskandani, M., Acriflavine-loaded solid lipid nanoparticles: preparation, physicochemical characterization, and anti-proliferative properties. Pharm Dev Technol 26, 934-942 (2021).

[15] Vaghasiya, K., Ray, E., Singh, R., Jadhav, K., Sharma, A., Khan, R., Katare, O. P., Verma, R. K., Efficient, enzyme responsive and tumor receptor targeting gelatin nanoparticles decorated with concanavalin-A for site-specific and controlled drug delivery for cancer therapy. Materials Science and Engineering: C 123, 112027 (2021).

[16] Karimian-Shaddel, A., Dadashi, H., Mashinchian, M., Mohabbat, A., Nazemiyeh, A. R., Vandghanooni, S., Eskandani, M., Codelivery of metformin and methotrexate with optimized chitosan nanoparticles for synergistic triple-negative breast cancer therapy in vivo. Int J Pharm 667, 124897 (2024).

[17] Zhang, D., Liu, L., Wang, J., Zhang, H., Zhang, Z., Xing, G., Wang, X., Liu, M., Drug-loaded PEG-PLGA nanoparticles for cancer treatment. Frontiers in pharmacology 13, 990505 (2022).

[18] Rouhi, A. A., Valizadeh, A., Sedghizadeh, N., Beba, L., Dadashi, H., Kazempour, M., Adibkia, K., Vandghanooni, S., Eskandani, M., Targeted therapy of gastric cancer with gingerol-loaded hyaluronic acid/PEG-coated PLGA nanoparticles: Development and physicochemical evaluation. J Drug Deliv Sci Technol 97, 105734 (2024).

[19] Zamanlu, M., Eskandani, M., Barar, J., Jaymand, M., Pakchin, P. S., Farhoudi, M., Enhanced thrombolysis using tissue plasminogen activator (tPA)-loaded PEGylated PLGA nanoparticles for ischemic stroke. J Drug Deliv Sci Technol 53, 101165 (2019). 1

[20] Vilas-Boas, V., Vinken, M., Hepatotoxicity induced by nanomaterials: mechanisms and in vitro models. Arch Toxicol 95, 27-52 (2021).

[21] Thomas, J., Kumar, V., Sharma, N., John, N., Umesh, M., Huligowda, L. K. D., Kaur, K., Utreja, D., Recent approaches in nanotoxicity assessment for drug delivery applications: challenges and prospects. Med Drug Discov 25, 100204 (2025).

[22] Bashir, S. M., Ahmed Rather, G., Patrício, A., Haq, Z., Sheikh, A. A., Shah, M. Z. u. H., Singh, H., Khan, A. A., Imtiyaz, S., Ahmad, S. B., Chitosan nanoparticles: a versatile platform for biomedical applications. Materials 15, 6521 (2022).

[23] Dadashi, H., Nazemiyeh, A. R., Karimian-Shaddel, A., mashinchian, M., Mohabbat, A., Faragheh, S. K., Vandghanooni, S., Eskandani, M., Enhancing ovarian cancer treatment: Synergistic effects of methotrexate (Methotrexate)- and quercetin-loaded chitosan nanoparticles. Carbohydr Polym Technol Appl 8, 100619 (2024).

[24] Martinez Junior, A. M., de Souza, R. H. F. V., Petronio, M. S., Martins, G. O., Fernandes, J. C., Benderdour, M., Tiera, V. A. O. d., Tiera, M. J., Double-grafted chitosans as siRNA nanocarriers: effects of diisopropylethylamine substitution and labile-PEG coating. J Nanostruct Chem 13, 605-624 (2023).

[25] Dadashi, H., Mashinchian, M., Karimian-Shaddel, A., Mohabbat, A., Vandghanooni, S., Eskandani, M., Jahanban-Esfahlan, R., Chitosan nanoparticles loaded with metformin and digoxin synergistically inhibit MCF-7 breast cancer cells through suppression of NOTCH-1 and HIF-1α gene expression. Int J Biol Macromol 287, 138418 (2025).

[26] Wang, J., Wang, J., Zhang, J., Ye, H., Wang, D., Tao, L., Yao, Y., Chen, Y., Shen, X., Bimetallic chitosan/hyaluronic acid nanoparticles self-amplify ferroptosis/cuproptosis in triple-negative breast cancer. Int J Biol Macromol 308, 142535 (2025).

[27] Zhang, Y., Li, Y., Ma, J., Wang, X., Yuan, Z., Wang, W., Convenient preparation of charge-adaptive chitosan nanomedicines for extended blood circulation and accelerated endosomal escape. Nano research 11, 4278-4292 (2018).

[28] Ashrafizadeh, M., Zarrabi, A., Hushmandi, K., Hashemi, F., Rahmani Moghadam, E., Raei, M., Kalantari, M., Tavakol, S., Mohammadinejad, R., Najafi, M., Progress in natural compounds/siRNA co-delivery employing nanovehicles for cancer therapy. ACS Comb Sci 22, 669-700 (2020).

[29] Liu, K., Chen, W., Yang, T., Wen, B., Ding, D., Keidar, M., Tang, J., Zhang, W., Paclitaxel and quercetin nanoparticles co-loaded in microspheres to prolong retention time for pulmonary drug delivery. Int J Nanomedicine 12, 8239-8255 (2017).

[30] Saroj, S., Us, P., Patil, S., Paul, D., Saha, S., Ali, A., Pal, S., Lochab, B., Rakshit, T., Herb extracellular Vesicle-Chitosan-PEGylated graphene oxide conjugate delivers estrogen receptor α targeting

siRNA to breast cancer cells. ACS Appl Bio Mater 7, 2741-2751 (2024).

[31] Naeem, A. G., Fawzi, S. F., Elmorsi, R. M., George, M. Y., Paclitaxel-induced adverse effects: insights into multi-organ toxicities and molecular mechanisms. Naunyn-Schmiedeberg's Arch Pharmacol 398, 1-30 (2025).

[32] Zhang, M., Lotfollahzadeh, S., Elzinad, N., Yang, X., Elsadawi, M., Gower, A. C., Belghasem, M., Shazly, T., Kolachalama, V. B., Chitalia, V. C., Alleviating iatrogenic effects of paclitaxel via antiinflammatory treatment. Vasc Med 29, 369-380 (2024).

[33] Azeem, M., Hanif, M., Mahmood, K., Ameer, N., Chughtai, F. R. S., Abid, U., An insight into anticancer, antioxidant, antimicrobial, antidiabetic and anti-inflammatory effects of quercetin: A review. Polym Bull (Berlin) 80, 241-262 (2023).

[34] Liu, L., Tong, Q., Liu, S., Cui, J., Zhang, Q., Sun, W., Yang, S., ZEB1 upregulates VEGF expression and stimulates angiogenesis in breast cancer. PLoS One 11, e0148774 (2016).

[35] Li, Q., Ma, Z., Liu, Y., Kan, X., Wang, C., Su, B., Li, Y., Zhang, Y., Wang, P., Luo, Y., Low doses of paclitaxel enhance liver metastasis of breast cancer cells in the mouse model. The FEBS journal 283, 2836-2852 (2016).

[36] Zamora, A., Alves, M., Chollet, C., Therville, N., Fougeray, T., Tatin, F., Franchet, C., Gomez-Brouchet, A., Vaysse, C., Martinez, L. O., Paclitaxel induces lymphatic endothelial cells autophagy to promote metastasis. Cell Death Dis 10, 956 (2019).

[37] Saadh, M. J., Ahmed, H. H., Chandra, M., Al-Hussainy, A. F., Hamid, J. A., Mishra, A., Taher, W. M., Alwan, M., Jawad, M. J., Al-Nuaimi, A. M. A., Therapeutic effects of quercetin in oral cancertherapy: a systematic review of preclinical evidence focused on oxidative damage, apoptosis and anti-metastasis. Cancer Cell Int 25, 66 (2025).

[38] Bi, X., Lou, P., Song, Y., Sheng, X., Liu, R., Deng, M., Yang, X., Li, G., Yuan, S., Zhang, H., Msi1 promotes breast cancer metastasis by regulating invadopodia-mediated extracellular matrix degradation via the Timp3–Mmp9 pathway. Oncogene 40, 4832-4845 (2021).

[39] Wen, J., Cao, X., Zhou, B., Yang, F., Wang, X., Li, Y., Zhao, X., Mei, J., Zhu, W., Sun, L., GC-MSCs transcriptionally upregulate SALL4 in gastric cancer through miR-4669/TIMP3/β-catenin signaling. Cell Signal 130, 111668 (2025).

[40] Banerjee, P., Xiao, G.-Y., Tan, X., Zheng, V. J., Shi, L., Rabassedas, M. N. B., Guo, H.-f., Liu, X., Yu, J., Diao, L., The EMT activator ZEB1 accelerates endosomal trafficking to establish a polarity axis in lung adenocarcinoma cells. Nat Commun 12, 6354 (2021).

[41] Dong, D., Zhou, Z., Zhu, M., Hou, Z., Chen, M., Gong, J., Zhao, X., Yan, A., Liang, H., Yin, Y., STN1 facilitates metastasis by promoting transcription of EMT-activator ZEB1 in pancreatic cancer. Nat Commun 16, 7815 (2025).

[42] Dadashi, H., Nazemiyeh, A. R., Karimian-Shaddel, A., Mohabbat, A., Faragheh, S. K., Vandghanooni, S., Eskandani, M., Enhancing ovarian cancer treatment: Synergistic effects of methotrexate (Methotrexate)- and quercetin-loaded chitosan nanoparticles. Carbohydrate Polymer Technologies and Applications 8, 100619 (2024).

[43] Eidet, J. R., Pasovic, L., Maria, R., Jackson, C. J., Utheim, T. P., Objective assessment of changes in nuclear morphology and cell distribution following induction of apoptosis. Diagn Pathol 9, 1-9 (2014).

[44] Wang, Y., Yu, H., Wang, S., Gai, C., Cui, X., Xu, Z., Li, W., Zhang, W., Targeted delivery of quercetin by nanoparticles based on chitosan sensitizing paclitaxel-resistant lung cancer cells to paclitaxel. Materials Science and Engineering: C 119, 111442 (2021).

[45] Jardim, K. V., Siqueira, J. L. N., Báo, S. N., Parize, A. L., In vitro cytotoxic and antioxidant evaluation of quercetin loaded in ionic cross-linked chitosan nanoparticles. J Drug Deliv Sci Technol 74, 103561 (2022).

[46] Son, G.-H., Lee, B.-J., Cho, C.-W., Mechanisms of drug release from advanced drug formulations such as polymeric-based drug-delivery systems and lipid nanoparticles. Journal of Pharmaceutical Investigation 47, 287-296 (2017).

[47] Vella-Zarb, L., Baisch, U., Dinnebier, R. E., Small molecule, big difference: The role of water in the crystallization of paclitaxel. J Pharm Sci 102, 674-683 (2013).

[48] Kitamura, M., Murakami, K., Yamada, K., Kawai, K., Kunishima, M., Binding of sulforhodamine B to human serum albumin: a spectroscopic study. Dyes Pigm 99, 588-593 (2013).

[49] Oguntade, A. S., Al-Amodi, F., Alrumayh, A., Alobaida, M., Bwalya, M., Anti-angiogenesis in cancer therapeutics: the magic bullet. Journal of the Egyptian National Cancer Institute 33, 1-11 (2021).

[50] Sonin, D., Pochkaeva, E., Zhuravskii, S., Postnov, V., Korolev, D., Vasina, L., Kostina, D., Mukhametdinova, D., Zelinskaya, I., Skorik, Y., Biological safety and biodistribution of chitosan nanoparticles. Nanomaterials 10, 810 (2020).

[51] Ranasinghe, L., Cotogno, P., Ledet, E., Bordlee, B., Degeyter, K., Nguyen, N., Steinberger, A., Manogue, C., Barata, P., Lewis, B. E., Relationship between serum markers and volume of liver metastases in castration-resistant prostate cancer. Cancer Treatment and Research Communications 20, 100151 (2019).

[52] Fabiani, I., Panichella, G., Aimo, A., Grigoratos, C., Vergaro, G., Pugliese, N. R., Taddei, S., Cardinale, D. M., Passino, C., Emdin, M., Subclinical cardiac damage in cancer patients before chemotherapy. Heart Fail Rev 27, 1-14 (2022)